AN OPTIMIZED MASS VALUE OF DARK MATTER PARTICLES BASED ON ULTRA-HIGH-ENERGY COSMIC RAYS

A Thesis Submitted to the College of

Graduate Studies and Research

In Partial Fulfillment of the Requirements

For a Master's Degree in Science

From the Department of Physics and Engineering Physics

University of Saskatchewan

Saskatoon

By

KARLA M. HOPP

Keywords: UHECR, WIMPZILLA, ultra high energy cosmic rays, dark matter

PERMISSION TO USE

In presenting this thesis in partial fulfilment of the requirements for a Postgraduate degree from the University of Saskatchewan, I agree that the Libraries of this University may make it freely available for inspection. I further agree that permission for copying of this thesis in any manner, in whole or in part, for scholarly purposes may be granted by the professor or professors who supervised my thesis work or, in their absence, by the Head of the Department or the Dean of the College in which my thesis work was done. It is understood that any copying or publication or use of this thesis or parts thereof for financial gain shall not be allowed without my written permission. It is also understood that due recognition shall be given to me and to the University of Saskatchewan in any scholarly use which may be made of any material in my thesis.

Requests for permission to copy or to make other use of material in this thesis in whole or part should be addressed to:

Head of the Department of Physics and Engineering Physics
University of Saskatchewan
Saskatoon, Saskatchewan, S7N 5E2

ABSTRACT

Though the arrival directions of ultra-high-energy cosmic rays (UHECRs) are distributed in a relatively isotropic manner, there is evidence of small-scale anisotropy. This, combined with the detection of cosmic rays with energies above the GZK cut-off, has motivated us to further investigate the idea that UHECRs are the result of a top-down mechanism involving the annihilation of superheavy dark matter particles in our galactic halo. To more precisely characterize the nature of dark matter, we have endeavoured to apply two different models to the leading UHECR spectra, namely those from the AGASA, High Resolution Fly's Eye, and Pierre Auger Collaborations. First, we attempt a non-linear, least-squares fit of the particle physics fragmentation function to the spectra. Second, we propose that the observed cosmic ray spectrum above 3.5×10^{18} eV is the superposition of flux from two different sources: bottom-up acceleration via a simple power-law relation at lower energies and scattered particles from dark matter annihilation governed by fragmentation functions at higher energies. We find that while the former model does not provide a satisfactory fit to observatory data, the latter yields reduced χ^2 values between 1.14 and 2.6. From the fragmentation function component of our second model, we are able to extract estimates of dark matter particle mass. We find values of $(1.2 \pm 0.6) \times 10^{21}$ eV, $(5.0 \pm 4.3) \times 10^{20}$ eV, and $(2.6 \pm 1.5) \times 10^{21}$ eV respectively for the AGASA, HiRes, and Pierre Auger data, which agree with earlier predictions based on a cosmological analysis of non-thermal particle production in an inflationary universe. Furthermore, we verify that the dark matter particle densities required by our two-source model are in line with current CDM theory.

ACKNOWLEDGMENTS

I thank my supervisor, Dr. Rainer Dick, for agreeing to take a chance on a dark horse, for sharing his extensive knowledge and wisdom, and for his tireless encouragement and support. I am grateful to the members of my committee, Dr. Alexander Moewes, Dr. Robert Pywell, Dr. Jacek Szmigielski, and Dr. Kaori Tanaka for their consideration of this work and for their thoughtful suggestions along the way. I thank my parents for instilling in me the desire for knowledge and the quest for excellence. I would also like to thank Marj Granrude, Michelle Bedier, Debbie Parker, and Clay Cederstrand for all of their help and humour.

I am grateful to the Natural Sciences and Engineering Research Council of Canada, the Canadian Council of Professional Engineers TD Meloche Monnex scholarship, and the University of Saskatchewan Graduate and Canadian Merit scholarships for funding this work.

To Mike, who continually helps me to learn about what is important in life, and without whom I would have never survived my first year of graduate studies. Thank you for your patience, understanding, and inspiration.

TABLE OF CONTENTS

PERMISSION TO USE i
ABSTRACT ii
ACKNOWLEDGMENTS iii
TABLE OF CONTENTS v
LIST OF TABLES vii
LIST OF FIGURES viii
LIST OF ABBREVIATIONS AND VARIABLES x
Chapter 1 INTRODUCTION 1
Chapter 2 BACKGROUND 3
2.1 Dark Matter 3
2.1.1 What is Dark Matter? 3
2.1.2 Evidence of Existence 3
2.1.3 Candidates 5
2.1.4 Modelling the Universe - The ΛCDM Model 6
2.2 Ultra-High-Energy Cosmic Rays 9
2.2.1 Overview 9
2.2.2 Origins of Cosmic Rays and the GZK Cut-off 9
2.2.3 Anisotropy in Arrival Directions? 13
Chapter 3 THEORY 16
3.1 UHECR Models 16
3.2 UHECRs as a Result of Dark Matter Annihilation 16
3.2.1 Justification 16
3.2.2 Constraints on Particle Mass 18
3.3 Fragmentation Functions 22
3.3.1 Motivation for the Use of Fragmentation Functions 22
3.3.2 Definition and Form of the Fragmentation Function 23
3.3.3 Universality and Extension to UHECR Regime 24
3.4 Calculation of UHECR Flux 25
3.5 Previous Work Related to UHECRs 27
Chapter 4 COLLECTION OF UHECR DATA 30

4.1 Extensive Air Showers (EAS) 30
4.2 Overview of Ground Detector Array Observatories 33
4.3 Overview of Air Fluorescence Observatories 35
4.4 Calculation of UHECR Spectrum from Air Shower Observations 38
4.5 Published Errors in UHECR Spectra 39
Chapter 5 ANALYSIS 42
5.1 Curve Fitting 42
5.2 χ^2-Square Fitting of UHECR Flux Data 42
5.3 The Levenberg-Marquardt Method 44
5.4 Error Estimation and Sensitivity Analysis 46
Chapter 6 RESULTS 48
6.1 Comparison of Models 48
6.2 Analysis of the AGASA Spectrum 48
6.3 Analysis of the HiRes Spectrum 51
6.4 Analysis of the Preliminary Auger Spectrum 53
6.5 Summary of Results 56
Chapter 7 DISCUSSION 57
Chapter 8 CONCLUSIONS 61
Chapter 9 RECOMMENDATIONS FOR FUTURE WORK 63
LIST OF REFERENCES 65
APPENDIX A: AGASA COLLABORATION SPECTRUM 71
APPENDIX B: HIGH RESOLUTION FLY'S EYE COLLABORATION MONOCULAR I SPECTRUM (June 1997 – February 2003) 73
APPENDIX C: PIERRE AUGER COLLABORATION SPECTRUM 74

LIST OF TABLES

Table 4.1: A comparison between the 68.27% confidence level intervals proposed by Feldman and Cousins (1998) and those predicted by a naïve use of Poisson statistics. 41

Table 6.1: Summary of parameters derived from fitting a combined low-energy power-law relation overlapped with a fragmentation function (Equation 3.40) to three independent UHECR spectra. 56

LIST OF FIGURES

Figure 2.1. High resolution simulation of the dark matter substructure in a galaxy cluster carried out by the Virgo Supercomputing Consortium using computers based at the Computing Centre of the Max-Planck Society in Garching and at the Edinburgh Parallel Computing Centre. The brighter the region, the more concentrated the dark matter. Data is publicly available at www.mpa-garching.mpg.de /galform/virgo/int_sims. 7

Figure 2.2. Flux of cosmic rays vs. energy. The straight dashed line represents a flux which varies with E^{-3}, as predicted by the Fermi theory of stochastic acceleration of charged particles in magnetic inhomogeneities (after S. Swordy, unpublished). 10

Figure 2.3. Mean energy loss length, $x_{loss}(E) = \frac{E}{dE/dx}$, due to adiabatic expansion (upper dotted curve), pair production (dash-dotted curve), hadron production (triple-dot-dashed curve). The hadron interaction length and neutron decay lengths are shown by the dashed and lower dotted curves respectively. Total mean loss length is given as a solid line (Stanev et al., 2000). 11

Figure 2.4: Most recently published spectrum from the AGASA observatory for events with zenith angles smaller than 45°. Open circles represent "well-contained" events whose cores are located at least 1 km inside the boundary of the array, while closed circles represent all events inside the array boundary. The numbers beside higher energy points represent the actual count of events in that energy bin. The highest and third-highest energy bins, depicted with error bars alone, are the 90% confidence level limits for that bin though no events were recorded by AGASA during the observation period. The dashed line is the expected spectrum for uniformly distributed, extragalactic sources, illustrating where the GZK cut-off should be (Takeda et al., 2003). 12

Figure 2.6. The arrival directions of cosmic rays with energies above 10^{19} eV, in equatorial coordinates. Dots, open circles, and open squares represent energies of 1 to 4×10^{19} eV, 4 to 10×10^{19} eV, and $> 10^{20}$ eV, respectively (Takeda et al., 1999). 14

Figure 2.7. AGASA Collaboration map of UHECR arrival directions in equatorial coordinates. Open circles and squares are defined as in Figure 2.6. Blue and purple-filled circles represent doublets and triplets respectively. 15

Figure 3.1: Annihilation of two WIMPZILLA particles, resulting initially in two jets of energy M_x which later fragment further. 22

Figure 4.1: The electromagnetic component present in all particle showers. (Adapted from www.gae.ucm.es) 31

Figure 4.2: Shower produced by proton or heavier nuclei primaries, containing both hadronic and electromagnetic components. (Adapted from www.gae.ucm.es) 31

Figure 4.3: Representation of an inclined shower, showing the shower front reaching the detectors at different times (www.auger.org/admin/ powerpoint.html). 34

Figure 4.4: Scintillation detectors are denoted by dots, while the radius of the surrounding circle is proportional to the detected particle density. The computed shower axis is indicated by the cross and the shower direction by the arrow (Sakaki et al., 2001). 34

Figure 4.5: Representation of the dual EAS detecting systems at the Pierre Auger Observatory. 36

Figure 4.6: Azimuth vs elevation of triggered photomultiplier tubes with a fit of shower-detector plane (Abbasi[1] et al., 2005). 37

Figure 4.7: Example of shower geometry relative to the HiRes detector (Abbasi[1] et al., 2005). 37

Figure 4.7: UHECR spectra from the AGASA Collaboration in diamonds (Takeda et al., 2003), the High Resolution Fly's Eye Collaboration in triangles (Bergman[2], 2005), and the Pierre Auger Collaboration in squares (Sommers, 2005). 40

Figure 6.1: Combined power-law and fragmentation function fit, given by smooth red line, to the most recently published AGASA UHECR spectrum, shown as a black segmented line with error bars. 49

Figure 6.2: Contribution of the two different spectral components to the overall UHECR spectrum reported by AGASA. 50

Figure 6.3: The smooth red line shows the superimposed power-law and fragmentation function fit to the HiRes Monocular I data collected from June 1997 to February 2003, shown as a segmented black line with error bars. 52

Figure 6.4: Contribution of the two spectral components included in our model to the overall UHECR spectrum published by HiRes. 53

Figure 6.5: Combined spectrum fit, given by smooth red line, to the preliminary Pierre Auger UHECR spectrum, shown as a black segmented line with error bars. 54

Figure 6.6: Individual components of the model spectrum compared to the Pierre Auger data. 55

LIST OF ABBREVIATIONS AND VARIABLES

$a(t)$	The time-dependent scale factor, which represents the relative expansion of the universe.
$A\Omega$	See aperture.
AGASA	Akeno Giant Air Shower Array: this Japanese observatory consisted of a 111 km^2 ground array of surface detectors designed to monitor secondary particle showers resulting from UHECRs.
aperture	For a cosmic ray observatory, the aperture, $A\Omega$, is the product of the ground-area covered with the solid angle of sky viewed.
Auger	Pierre Auger Observatory: the southern Auger Observatory (Argentina) employs both a 3000 km^2 ground array as well as four sites containing air fluorescence telescopes to monitor UHECR particle showers.
CDM	Cold Dark Matter: in this model, dark matter consists of hypothetical particles which are cold, i.e. non-relativistic at the beginning of the matter-dominated epoch and hence able to form gravitationally-bound clumps, collisionless, i.e. having very little interaction with itself or other matter, and long-lived, i.e. having a life-span longer than the current age of the universe.
CMB	Cosmic Microwave Background: the universe is permeated with microwave radiation having a density of ~400 photons/cm^3. Small variations in the CMB are indications of inhomogeneity in energy densities in the early universe.
EAS	Extensive Air Showers: a cascade of particles and/or electromagnetic radiation caused by the collision of a primary cosmic ray with a particle in the atmosphere.
exposure	For a cosmic ray observatory, the exposure is the aperture multiplied by the length of observation time.
FRW model	Friedmann-Robertson-Walker model: a cosmological model in which the geometry of spacetime is homogeneous and isotropic.
$g_{\mu\nu}$	In this work, $g_{\mu\nu}$ is the FRW metric, a symmetric, position-dependent matrix used to measure distances in spacetime.

GZK cut-off (bound)	Greisen-Zatsepin-Kuz'min cut-off: the theoretical upper-limit to the energy of cosmic rays arriving from distant sources (~4 $\times 10^{19}$eV) due to interaction with the CMB.
H	The Hubble parameter measures the expansion rate of the universe as a function of time.
$\mathbf{H}$	Hessian matrix: a $P \times P$ matrix used in the inverse-Hessian minimization method of curve fitting.
$\hbar$	Plank's constant, 6.582×10^{-16}eV·s.
HiRes	High Resolution Fly's Eye Observatory: this Utah-based observatory uses air fluorescence telescopes to observe scintillation tracks made by UHECR showers as they pass through the atmosphere
$J(E)$	Differential flux: the number of cosmic rays observed per ground area and solid angle of the sky for a given time in a given energy range [$m^{-2}\,sr^{-1}\,s^{-1}\,eV^{-1}$].
M_X	The rest mass energy of a super-heavy dark matter particle such that $M_X = m_X c^2$.
N_{cl}	Total number of dark matter particles in a subclump.
N_i	The number of cosmic ray events measured in the i-th energy bin.
n_X	The number density of dark matter particles.
PMT	Photomultiplier tube: an instrument that is sensitive to the detection of low levels of light and capable of multiplying the signals to useable levels.
SHDM	Superheavy dark matter.
UHECR	Ultra-High-Energy Cosmic Ray: a particle coming from an extra-terrestrial source having an energy roughly above 10^{18} eV.
WIMP	Weakly-Interacting Massive Particle: a candidate for dark matter, this thermal relic is thought to have a mass range from 10^9 to 10^{11}eV.
WIMPZILLA	A superheavy Weakly-Interacting Massive Particle thought to be a non-thermal relic of the early universe with a mass of

	10^{21} to 10^{23} eV.
χ_v^2	Reduced chi-squared: a measure of the goodness of fit of a model to a set of observations for which a value of 1 is considered to be an excellent fit.
$v\eta\xi$	The three unknowns remaining in the UHECR flux calculation (see Section 3.4) where v is 4 for Majorana particles or 1 otherwise, η is the ratio of core mass density of dark matter halo subclumps to the density of the sun, and ξ must be less than one due to unitarity bound constraints.
$\langle \sigma_A v \rangle$	The thermally averaged cross-section for superheavy dark matter particles.

Chapter 1 INTRODUCTION

Currently, two of the most compelling puzzles in astroparticle physics are the characterization of dark matter and the explanation of the origin of ultra-high-energy cosmic rays (UHECRs). Some theories postulate that the two phenomena are linked—that UHECRs are the result of dark matter particle decay or annihilation. In order for these scenarios to be feasible, dark matter must meet a number of constraints that are largely imposed by UHECR observations. Firstly, a substantial fraction of dark matter must be composed of super-heavy, weakly-interacting particles. At the beginning of the universe, these exotic particles must have been created with adequately long lifetimes and in large enough quantities to be able to produce ultra-high-energy cosmic rays at the frequencies observed today. Sufficient concentrations of dark matter must also be distributed within galaxy-containing regions of space to account for the nearly isotropic arrival directions of UHECRs. Finally, dark matter particles must have a high enough rest mass such that the decay or annihilation products are capable of matching the very highest energy cosmic rays.

Previous investigations of dark matter particle characteristics have tended to give a range of possible mass values that extend over several orders of magnitude (Griest and Kamionkowski, 1990; Kolb et al., 1999; Fodor and Katz, 2001; Hui, 2001; Blasi et al., 2002; Sarkar and Toldrá, 2002; Dick et al., 2005). The goal of this thesis is to make a more precise mass estimation for non-thermal dark matter particles using particle physics theory. This alternate calculation of dark matter particle mass is undertaken to further refine or discount the proposal that UHECRs are the result of dark matter annihilation. The topic is a timely one,

since within a few years the southern Pierre Auger Observatory in Argentina should accumulate enough data to address the validity of all prevalent theories on the origin of UHECRs (Dick et al., 2005).

In order to acquaint the reader with the foundations of the topic, Chapter 2 provides an overview of existing ideas about dark matter and UHECRs and examines some of the competing views that exist in areas affecting the project. Chapter 3 discusses the theory of dark matter annihilation as a source of UHECRs and motivates the particle physics approach to the calculation of particle mass. Chapter 4 provides the pertinent details of UHECR observation and methods used to calculate cosmic ray spectra from these observations. The analysis methods that we applied to the spectra are explained in Chapter 5, while Chapter 6 gives the results of the analysis of data from the three most prominent UHECR observatories. The final chapters provide discussion and conclusions for this work, as well as suggestions for future directions in the research.

Chapter 2 BACKGROUND

2.1 Dark Matter

2.1.1 What is Dark Matter?

Dark matter is a theoretical construct for explaining observed anomalies in the behaviour of luminous celestial bodies. In many ways, the current problem of dark matter resembles past puzzles arising from unseen planets. Astronomers have observed unusual behaviour, on both galactic and cosmological scales, that can only be explained by the existence of a significant amount of unseen, "dark matter," or by modifying the laws of gravity. Dark matter is thought to comprise about 90% of the matter in the universe, but since it neither emits nor reflects radiation with the possible exception of fragmentation products, it can only be detected indirectly.

2.1.2 Evidence of Existence

The case for the existence of dark matter has been slowly building for many years. As early as 1933, Fritz Zwicky measured the velocity dispersion of galaxies in the nearby Coma cluster. He then used the virial theorem to determine that the density of the cluster should be 400 times greater than that calculated from luminous matter (van den Bergh, 1999). Three years later, Sinclair Smith made similar observations on the Virgo cluster. Smith found that some galaxies had velocities in excess of his calculated escape velocity for the cluster and yet these galaxies remained bound. He postulated that there must be a vast amount of internebular material within the cluster.

Since these early beginnings, more sophisticated tests of dark matter have been performed. It was expected that galaxies, like planets, would roughly follow Newton's laws, which state that the circular velocity, *v(r),* of a body depends only on its radial distance from the orbital centre and on the total mass contained within the orbit, $M(r) = 4\pi \int \rho(r')r'^2\, dr'$, where $\rho(r)$ is the density distribution function (G. Bertone et al., 2005). The graph of the circular velocity of the stars in a galaxy versus their distance from the galactic centre is known as a rotation curve. The expectation is that this velocity may be estimated by equating centrifugal and gravitational forces,

$$v(r) = \sqrt{\frac{GM(r)}{r}} \tag{2.1}$$

Rather than finding that the velocity of the outer portion of a galaxy decreases with $r^{-½}$ as predicted by Equation 2.1, astronomers have observed that the velocity approximately levels off to a constant. This implies the existence of a dark matter halo whose total mass varies with radius, and whose density varies with $\sim 1/r^2$.

Anomalies in strong gravitational lensing have also been held up as evidence for the existence of dark matter and a clue to its structure. A study performed by Mao and Schneider (1998) examined quasars that were multiply imaged by intervening galaxies. They found that modelling the gravitational potential for the lensing galaxy by a simple, smooth distribution could not reproduce the observed images for some quasars. They suggested that the presence of dark matter substructure or clumps in the lensing galaxy could explain the anomalies. Chiba (2002) later expanded this investigation and also determined that other known objects, such as globular clusters and luminous dwarf satellites, could not explain the lensing behaviour observed.

There are indications that dark matter may not be composed of any type of particle that we are familiar with. A baryon density large enough to account for all of the matter in the universe would lead to anisotropies in cosmic microwave background (CMB) radiation that are much larger than observed. Data from the

Wilkinson Microwave Anisotropy Probe (WMAP) has been used to map CMB anisotropy to new levels of accuracy. The preliminary findings of the WMAP team are that only 4.4% of the energy in the universe is composed of ordinary baryonic matter while dark matter accounts for 22% (C. L. Bennett et al., 2003). Since baryonic matter only comprises a small fraction of the matter in the universe, the question then becomes: what makes up the rest?

2.1.3 Candidates

There is a wide range of hypotheses about the composition of dark matter. Big Bang nucleosynthesis (BBN) makes predictions about the baryonic density of the universe which have been found to be in good agreement with observation. The success of BBN therefore restricts the amount of baryonic dark matter to a fraction of what is required. Despite evidence that baryonic density is constrained, some still speculate that dark matter is baryonic, as this would not require changes to the standard model. Theories for baryonic dark matter candidates range from MAssive Compact Halo Objects (MACHOS) on a galactic scale, such as white dwarfs, dim infrared stars, brown dwarfs and planets, to objects such as low surface-brightness galaxies, neutron stars, black holes, gas, and dust clouds on a cosmologic scale.

Cold dark matter (CDM) theory involving hypothetical, non-baryonic particles has emerged as a favourite in the past decade. The proposals for non-baryonic dark matter candidates are also very diverse. For a while, neutrinos were regarded as a very promising possibility, particularly because they "have the undisputed virtue of being known to exist" (Bergström, 2000). However, recent constraints on the upper limit of neutrino mass suggest that neutrinos can only make up a small fraction of dark matter (Bertone et al., 2005). Neutrinos would also be "hot" dark matter and thus could not have participated in the formation of structure in the universe. Numerous other hypotheses for exotic dark matter particles exist, some of which are: axions, weakly interacting massive particles (WIMPS) such as neutralinos and other supersymmetric particles, superheavy

dark matter particles (WIMPZILLAs or SHDM), and Kaluza-Klein states resulting from extra dimensions. WIMPZILLAs are of particular interest because they may not only solve the puzzle of dark matter composition, but WIMPZILLA decay or annihilation could also be the source of the highest energy cosmic rays that strike the Earth.

WIMPZILLAs are thought to be relics of the early universe, produced at the end of inflation through a number of possible mechanisms. They have an extremely high mass $\approx 10^{22}$ eV (Kolb et al., 1999), though literature values range from 10^{18} to 10^{27} eV (Griest and Kamionkowski, 1990; Fodor and Katz, 2001; Hui, 2001; Blasi et al., 2002; Sarkar and Toldrá, 2002; Dick et al., 2005).

2.1.4 Modelling the Universe - The ΛCDM Model

Though different research teams use different computer programs and assumptions to create their view of the universe, current cosmological models, called "ΛCDM" models, are based on an inflationary universe with CDM particles and a cosmological constant, Λ. In this model, the structure of the universe starts out as primordial density fluctuations that eventually form CDM clumps. These clumps collapse and then undergo a series of mergers with other clumps, eventually forming large, massive, dark matter haloes. The haloes then act as hosts to the visible structure in the universe, from galaxies to clusters (Hayashi et al., 2003).

An inflationary universe has a flat geometry, i.e., a critical density of 1. In ΛCDM models, matter is considered to make up about 0.3 of the critical density, with baryonic matter forming only a small fraction of this. A cosmological constant of ~0.7 composes the remainder of the critical density. Dark matter particles are modelled as being long-lived, cold, and collisionless: "long-lived" because they have a lifetime greater than the present age of the universe; "cold," as they were non-relativistic early in the formation of the universe and soon formed gravitational clusters; and "collisionless" since the interaction of dark

matter particles with themselves as well as with ordinary matter is considered negligible at the densities found in dark matter halos (Ostriker and Steinhardt, 2003).

The ΛCDM model has had many successes. Predictions derived from N-body simulations of the model agree with many observations, including the characteristic fluctuations in the CMB, measurements of the brightness of distant supernovae, and the age of the universe as estimated from the oldest stars (Bahcall et al., 1999; Tasitsiomi, 2003). One of the most impressive features of the ΛCDM model is that it predicts an abundance of substructure that agrees with the observed large-scale (≥ 1 Mpc) structure of galaxy clusters, as shown in Figure 2.1.

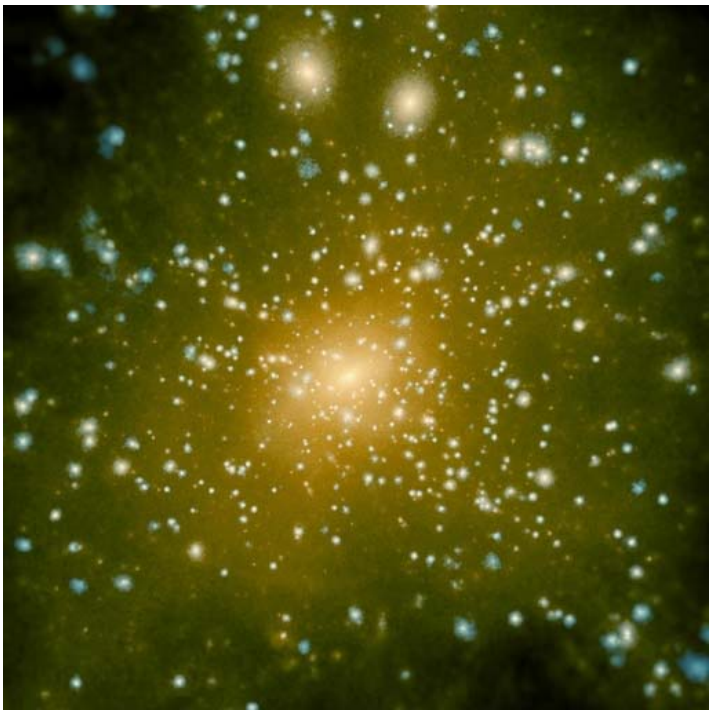

Figure 2.1. High resolution simulation of the dark matter substructure in a galaxy cluster carried out by the Virgo Supercomputing Consortium using computers based at the Computing Centre of the Max-Planck Society in Garching and at the Edinburgh Parallel Computing Centre. The brighter the region, the more concentrated the dark matter. Data is publicly available at www.mpa-garching.mpg.de /galform/virgo/int_sims.

Much work has been done to establish the characteristics of the dark matter haloes which host galaxies and clusters, but a consensus on how to describe their structure has not yet been reached. Early works tended to represent the dark

matter density in haloes with an isothermal density distribution; that is $\rho \propto r^{-2}$ where r is the radial distance from the centre of the host halo. In the last decade, many numerical studies have been performed on the density profiles of CDM haloes. Though results vary, the studies all tend to agree on three basic points.

1) The large-scale density of dark matter is highest at the centre of the halo, and is likely even more dense than the isothermal profile, with $\rho \propto r^{-1.5}$ or higher.
2) Density decreases with radial distance until it is less than isothermal near the edge of the halo ($\rho \propto r^{-3}$).
3) The profile is not entirely smooth, but rather there are embedded clumps, or subclumps, of dark matter.

The most often cited shortcoming (even called a "crisis") of the ΛCDM model is that it appears to drastically over-predict the amount of substructure on smaller scales. In early N-body simulations using the ΛCDM model, Klypin et al. (1999) noticed that their model of our "Local Group" of galaxies had 50 to 100 satellites while only 12 satellites have actually been observed. Moore[1] et al. (1999) found that substructure was over-predicted by a factor of 50. Though Moore et al. used different modelling software, they also had much higher resolution (a greater number of particles representing a given mass) in their N-body simulation than Klypin et al.

The over-prediction of substructure has lead to speculation about the existence of dark satellites, or subclumps, composed either entirely of dark matter or having very little luminous matter. Hayashi et al. (2003) predicted that less than 1 in 10 subclumps is inhabited by a luminous satellite. Similarly, Dalal and Kockanek (2002) speculated that the number of visible satellites is only a lower bound for the possible number of satellites in the Local Group. Since gravitational lensing provides information about mass distribution that does not depend upon the luminosity of the lensing galaxy, they developed a technique to estimate the satellite population of lens galaxies. Their analysis of numerous lenses predicted

that 0.6 to 7% of the mass of a halo is in the form of substructure, significantly higher than the 0.01 to 0.1% mass in visible substructures. CDM models have predicted that anywhere from 2 to 15% of the galactic mass is substructure (Springel et al., 2001; Stoehr et al., 2002; Hayashi et al., 2003).

Recent N-body simulations have employed increasingly more powerful parallel-computing facilities which have facilitated increased resolution. These studies find still greater quantities of subclumps (several hundred times more than observed) and even evidence of substructure within the subclumps (Moore et al., 2001). The rate of increase of the number of subclumps has been shown to decrease with increasing resolution (Ghigna et al., 2000; V. Springel et al., 2001); thus there is some hope for convergence of subclump counts with high enough resolution. It has been suggested that sufficient computing power to achieve the requisite resolution is still several years away.

2.2 Ultra-High-Energy Cosmic Rays

2.2.1 Overview

Cosmic rays are particles that continually bombard the Earth, ranging in energy, E, from 10^9 eV to over 10^{20} eV. Figure 2.2 illustrates that cosmic ray flux generally depends upon the energy of the incoming particles, varying with $\sim E^{-2.7}$ for energies below the "knee" ($\sim 10^{15}$ eV), steepening to $\sim E^{-3}$ for energies between the knee and the "ankle" ($\sim 10^{18}$ eV), and slightly flattening again above the ankle (Dova et al., 2001). Cosmic rays with an energy above 10^{18} eV are dubbed "ultra-high-energy cosmic rays". The highest energy cosmic ray ever observed had an energy of $(3.2 \pm 0.9) \times 10^{20}$ eV and was detected by the Fly's Eye experiment, a precursor to High Resolution Fly's Eye (HiRes) in Utah (Bird et al., 1991).

2.2.2 Origins of Cosmic Rays and the GZK Cut-off

The study of UHECRs is particularly important for two reasons. Within the galaxy, there exists a magnetic field of a few micro Gauss, and it is estimated that intergalactic magnetic fields have a strength on the order of 10 nano Gauss

(Olinto, 2004). Lower-energy cosmic rays can be deflected by galactic and intergalactic magnetic fields and thus their arrival direction does not provide any information about the location of their sources. However, UHECRs have such high energies that their trajectories are not significantly bent by magnetic fields of this order. Thus they may be able to provide information about the location of cosmic ray sources.

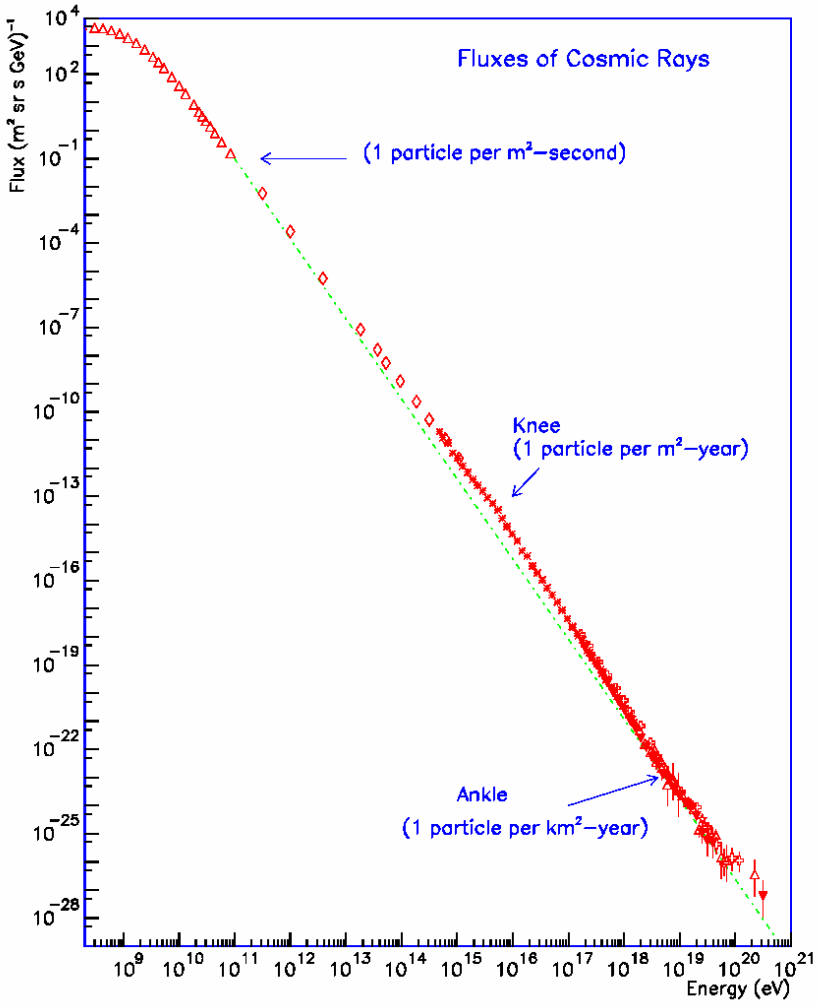

Figure 2.2. Flux of cosmic rays vs. energy. The straight dashed line represents a flux which varies with E^{-3}, as predicted by the Fermi theory of stochastic acceleration of charged particles in magnetic inhomogeneities (after S. Swordy, unpublished).

UHECRs are also of great interest due to the work done by Greisen, Zatsepin, and Kuz'min (Greisen, 1966; Zatsepin and Kuz'min, 1966). Considering protons, heavy nuclei, and photons as candidate particles for cosmic rays, they proposed

that there should be a significant change in the cosmic ray spectrum at ~4×10^{19} eV. The so-called GZK cut-off occurs because the universe is permeated with CMB radiation having a density of ~400 photons/cm^3. Low-energy particles are not appreciably affected when travelling through the CMB, but for particles having an energy above 4×10^{19} eV, the rate of reaction with the background radiation becomes significant, causing the particles to lose energy. Unless we are considering some sort of exotic particle which does not interact with the CMB, there is an energy-dependent limit to how far a charged ultra-high-energy particle can travel, as shown in Figure 2.3. Cosmic rays having an energy above 10^{20} eV must have originated not far from the Milky Way, i.e. within 60 Mpc. This value falls to 20 Mpc for the highest energy cosmic ray recorded ($3.2 \pm 0.9 \times 10^{20}$ eV) if the primary particle was a proton, lower still if the primary was a heavy nucleus or a photon (Sarkar and Toldrà, 2002).

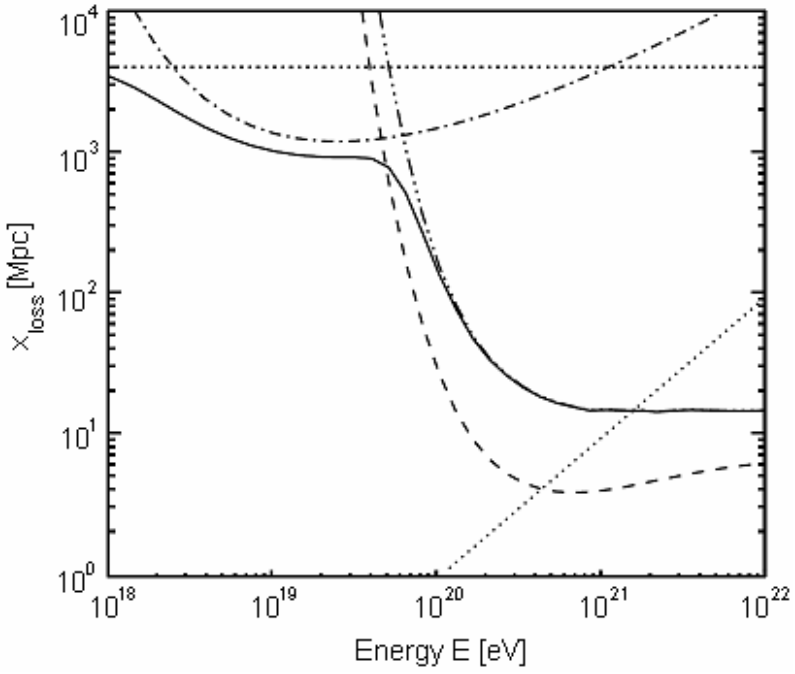

Figure 2.3. Mean energy loss length, $x_{loss}(E) = \dfrac{E}{dE/dx}$, due to adiabatic expansion (upper dotted curve), pair production (dash-dotted curve), hadron production (triple-dot-dashed curve). The hadron interaction length and neutron decay lengths are shown by the dashed and lower dotted curves respectively. Total mean loss length is given as a solid line (Stanev et al., 2000).

A controversy has arisen over whether UHECR data really exhibits a GZK cut-off or not. Due to the infrequent arrival of UHECRs (~1 per 100 km^2 per year), the number of recorded events to date is still quite small. For over a decade, the Akeno Giant Air Shower Array (AGASA) Observatory in Japan employed a 111 km^2 array of surface scintillation detectors to monitor particle showers resulting from UHECR collisions with atmospheric particles. Though their early work favoured the existence of a GZK cut-off (Yoshida et al., 1995), the AGASA Collaboration now reports that there is no cut-off in their UHECR spectrum, as shown in Figure 2.4 (Takeda et al., 1998, 2003). As of their last published spectrum, they find 65 events having energies > 4×10^{19} eV. The Yakutsk Extended Air Shower Array in Russia also reports a lack of GZK cut-off, having recorded a number of events above 4×10^{19} eV (Knurenko et al., 2005).

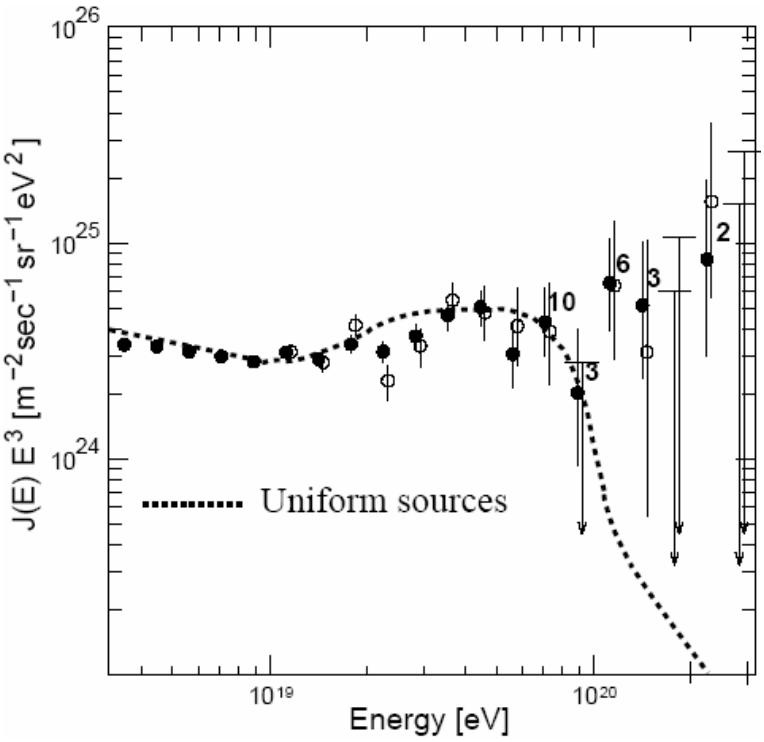

Figure 2.4: Most recently published spectrum from the AGASA observatory for events with zenith angles smaller than 45°. Open circles represent "well-contained" events whose cores are located at least 1 km inside the boundary of the array, while closed circles represent all events inside the array boundary. The numbers beside higher energy points represent the actual count of events in that energy bin. The highest and third-highest energy bins, depicted with error bars alone, are the 90% confidence level limits for that bin though no events were recorded by AGASA during the observation period. The dashed line is the expected spectrum for uniformly distributed, extragalactic sources, illustrating where the GZK cut-off should be (Takeda et al., 2003).

In contrast, the HiRes Collaboration reports a decrease in flux at ultra-high energies that is more consistent with the GZK cut-off (Westerhoff, 2004). This is ironic, perhaps, since Fly's Eye also lays claim to the highest energy cosmic ray event ever recorded. Their spectrum from June 1997 to February 2003 included 35 super-GZK events out of ~1600 UHECRs logged (Bergman[2], 2005). The HiRes experiment uses air fluorescence telescopes to observe scintillation tracks made by UHECR showers as they pass through the atmosphere on clear, moonless nights. The Monocular Fly's Eye, or HiRes-1, has been in operation since 1997 and has logged a quantity of cosmic ray events comparable to that of AGASA. However, the data sets for both experiments are still quite small and much more data needs to be collected for a statement about the existence of a GZK cut-off to become statistically significant. It is also necessary to develop an understanding of how the two different detection techniques affect the calculation of UHECR energies.

The Pierre Auger Observatory, which is nearing completion and has already begun data collection, aims to resolve these disputes. The Auger Observatory has both a grid of water Cherenkov surface detectors covering 27 times the area of AGASA as well as four sites containing fluorescence telescopes overlooking the grid. When possible, both observation techniques will be used to measure the same event so that discrepancies in the calculation of primary particle energies may be rectified. In addition, the much larger ground array will allow the collection of a data set having reliable statistics within just a few years. It is estimated that Auger will collect 60 events above 10^{20} eV per year and 6000 above 10^{19} eV, which should not only address the question of the presence of a GZK cut-off, but also resolve the question of whether there is anisotropy in UHECR arrival directions.

2.2.3 Anisotropy in Arrival Directions?

While the arrival directions of UHECRs appear to be distributed in a fairly uniform manner throughout the sky, as illustrated in Figure 2.6, the AGASA

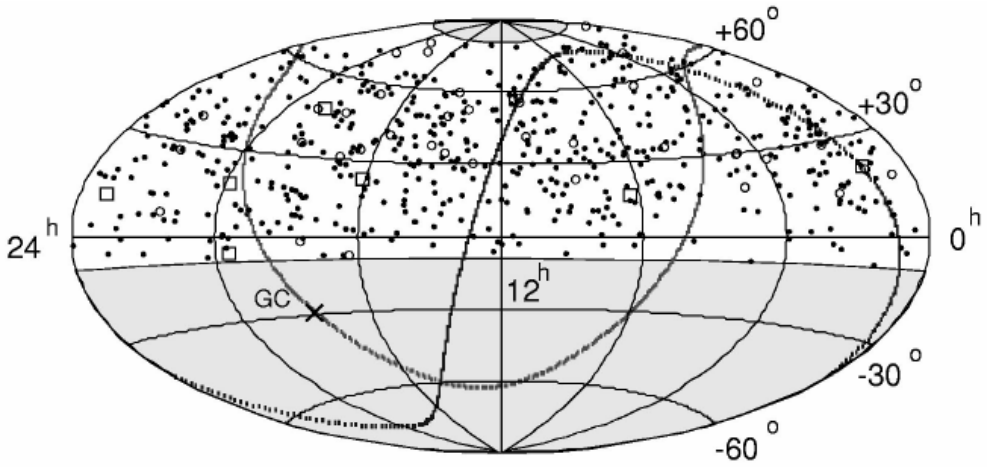

Figure 2.6. The arrival directions of cosmic rays with energies above 10^{19} eV, in equatorial coordinates. Dots, open circles, and open squares represent energies of 1 to 4×10^{19} eV, 4 to 10×10^{19} eV, and > 10^{20} eV, respectively (Takeda et al., 1999).

Collaboration has reported some small-scale anisotropy in cosmic rays with energies $\geq 4 \times 10^{19}$ eV (Takeda et al, 1999). AGASA has observed five instances where the arrival directions of two cosmic rays (doublets) are within 2.5° and one instance of a triplet cluster, as shown in Figure 2.7. There is a probability of less than 1% that these clusters would occur by chance in an isotropic distribution. Uchihori et al. (2000) increased their sample set to 92 UHECR events by examining the available data from four different surface array experiments in the northern hemisphere. They found 12 doublets and 2 triplets in the set, and agreed with AGASA's probability estimates. In contrast, the HiRes Collaboration does not find any anisotropy in their dataset (Westerhoff et al., 2004; Abbasi[2] et al., 2005). Farrar (2005) notes that one of the HiRes UHECR events ($E = 3.76 \times 10^{19}$ eV) is coincident with the AGASA triplet with a chance probability of only 10^{-3}. Farrar also examined HiRes observations in the 1 to 3×10^{19} eV energy range and found a fifth event arriving from the same direction. Because of the much larger number of events in this lower-energy data set, however, the probability of this occurring by chance increases to 1 in 6. Again, it is hoped that the Pierre Auger project will settle this dispute. The southern Auger observatory will also be able to test whether there is any anisotropy toward the

galactic centre; AGASA could not view the centre of the galaxy from its vantage point.

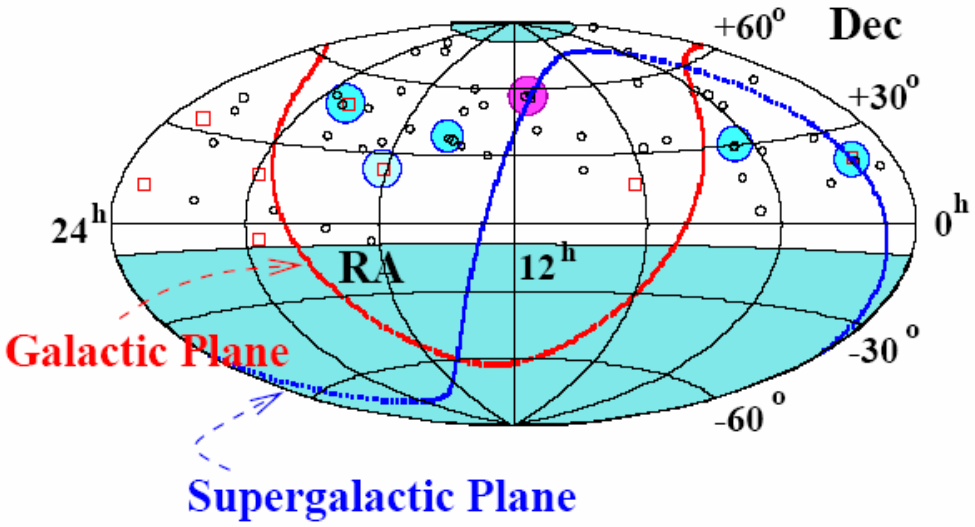

Figure 2.7. AGASA Collaboration map of UHECR arrival directions in equatorial coordinates. Open circles and squares are defined as in Figure 2.6. Blue and purple-filled circles represent doublets and triplets respectively.

Chapter 3 THEORY

3.1 UHECR Models

There are two prevalent theories about the origin of UHECRs: the bottom-up and top-down models. In the bottom-up model, particles are accelerated by large, energetic, astrophysical objects where strong shocks are found, such as Active Galactic Nuclei or Supernovas. Nagano and Watson (2000) consider the limit for bottom-up particle acceleration by an astrophysical object to be between 10^{20} and 10^{21} eV, though proponents of the top-down model argue against the feasibility of such energetic acceleration (e.g. Hillas, 1984; Sakaki et al., 2001). In the top-down model, UHECRs result from the decay or annihilation of heavy particles that were created in the early stages of the formation of the universe.

3.2 UHECRs as a Result of Dark Matter Annihilation

3.2.1 Justification

The bottom-up model for UHECR creation has the distinct benefit of not requiring that a new class of particles be accepted into the standard model. However, the bottom-up model is not without its own demands on the boundaries of known physics. It is very difficult to devise sufficiently efficient astrophysical mechanisms to accelerate particles to super-GZK energies and at the same time overcome collisional and radiation losses. Additionally, if one considers the GZK bound, then some of these accelerating objects must be less than 20 Mpc away from the Earth.

Another strike against the bottom-up model is that the arrival directions of UHECRs have been nearly isotropic to date, as discussed in Section 2.2.3. Large,

accelerating bodies would not only have to be nearby, but there would also have to be many of them, uniformly distributed around the Earth. The highest energy cosmic rays, those least affected by magnetic fields, have not been found to point back to any known candidate body.

On the merit of the AGASA spectrum, the restrictions imposed by the GZK cut-off led to the idea that UHECRs may result from the decay of super-heavy dark matter particles (Berezinsky et al., 1997). Decaying particles would be located in the galactic halo, well within the GZK cut-off distance. As decay would directly convert the rest mass of WIMPZILLA particles into UHECR energy, there would be no requirement for an acceleration mechanism, though it would be necessary for particle mass to be $\geq 10^{21}$ eV in order to account for the highest energy events. The difficulty with this proposal lies in finding a decay mechanism for such massive particles that proceeds slowly enough to allow a significant particle population to still exist today. If a suitable decay mechanism does exist, then the frequency of UHECR events should increase with dark matter density. N-body models predict that at least 85% of the dark matter near a galaxy is contained in a parent halo which smoothly decreases in density with increasing radial distance (refer to Section 2.1.4). Thus, cosmic rays from WIMPZILLA decay should exhibit a relatively smooth increase in the number of events as one looks from the outer edges of the galaxy toward its centre.

The AGASA Collaboration's findings of anisotropy in UHECR arrival directions combined with decay scenario problems provided the incentive for the theory that UHECRs are produced by the collisional annihilation of WIMPZILLAs (Blasi et al., 2002). Since reaction rate (i.e. change in number-density of the particles) depends upon annihilation cross section $\dot{n}_X \propto -n_X^2 \langle \sigma_A v \rangle$, and the unitarity bound states that the cross section decreases with increasing mass, $\sigma_A \propto m_X^{-2}$, such annihilating WIMPZILLA particles could still feasibly exist today. Only the highest-density subclumps in the galactic halo would have a sufficient concentration of dark matter to produce the observed UHECR flux due to the

small cross section. The means that the signature of UHECRs from annihilation would be quite different than that from decay: rather than a smoothly increasing distribution, ~1000 point-like sources should exist, increasing in density toward the galactic centre (Dick et al., 2005).

3.2.2 Constraints on Particle Mass

Dick et al. (2005) recently undertook a cosmological analysis of dark matter particle mass. The evolution equations of weakly coupled scalar fields in the inflationary universe were used to study the limitations of non-thermal particle production. This section summarizes the analysis performed.

The Friedmann-Robertson-Walker (FRW) metric in co-moving Cartesian coordinates,

$$ds^2 = -dt^2 + a^2(t)\left(d\mathbf{x}^2 + k\frac{(\mathbf{x}\cdot d\mathbf{x})^2}{1-k\mathbf{x}^2} \right) \tag{3.1}$$

has components

$$g_{00} = -1, \quad g_{0j} = 0, \quad g_{ij} = a^2(t)\left(\delta_{ij} + k\frac{x_i x_j}{1-kr^2} \right) \tag{3.2}$$

where ds^2 is a line element in four-dimensional FRW space, a is the time-dependent scale factor, $r^2 \equiv |\mathbf{x}|^2 \equiv \sum_{i=1}^{3} x_i^2$ (with $x^i \equiv x_i$ in this case), and $k = 0$ for flat space, -1 for an open universe, 1 for a closed universe.

Since $g^{ij}g_{jk} = \delta_k^i$, the components $g^{\mu\nu}$ of the inverse metric can be found as

$$g^{00} = -1, \quad g^{0j} = 0, \quad g^{ij} = \frac{1}{a^2(t)}\left(\delta^{ij} - kx_i x_j\right). \tag{3.3}$$

The action for a free scalar quantum field in curved space is

$$S = \int d^4x\, \mathcal{L} = \int d^4x \sqrt{-g}\left(-\frac{1}{2} g^{\mu\nu}\partial_\mu\phi\,\partial_\nu\phi - \frac{1}{2}m^2\phi^2 \right) \tag{3.4}$$

where $\mathcal{L}$ is the Lagrangian density, g is defined to be the determinant of $g_{\mu\nu}$, and the four volume element, $dv = d^4x\sqrt{-g}$. Substituting the FRW values for g and $g^{\mu\nu}$, and using the convention that $m \equiv \frac{m_X c^2}{\hbar} \equiv \frac{M_X}{\hbar}$, we find $\mathcal{L}$ to be

$$\mathcal{L} = \frac{a^3}{\sqrt{1-kr^2}}\left(\frac{1}{2}\dot{\phi}^2 - \frac{1}{2}a^2(\delta^{ij} - kx^i x^j)\partial_i\phi\,\partial_j\phi - \frac{1}{2}m^2\phi^2\right). \tag{3.5}$$

We may then solve the Euler-Lagrange equation of motion for a field,

$$\partial_\mu\left(\frac{\partial\mathcal{L}}{\partial(\partial_\mu\phi)}\right) - \frac{\partial\mathcal{L}}{\partial\phi} = 0 \tag{3.6}$$

to arrive at the equation of motion for a massive scalar field in an FRW background,

$$\ddot{\phi}(\mathbf{x},t) + 3\frac{\dot{a}(t)}{a(t)}\dot{\phi}(\mathbf{x},t) - \frac{1}{a^2(t)}\left[\left(\delta^{ij} - kx^i x^j\right)\partial_i\partial_j - 3kx^i\partial_i\right]\phi(\mathbf{x},t) + m^2\phi(\mathbf{x},t) = 0 \tag{3.7}$$

Since we are interested in studying particle creation, we must determine whether there is a violation of the energy conservation law,

$$\partial_\mu\left(\sqrt{-g}\,T^{\mu\nu}\right) = 0 \tag{3.8}$$

where $T^{\mu\nu}$ is the energy-momentum tensor, with

$$T_{\mu\nu} = \frac{-2}{\sqrt{-g}}\frac{\partial\mathcal{L}}{\partial g^{\mu\nu}} = \partial_\mu\phi\,\partial_\nu\phi - \frac{1}{2}g_{\mu\nu}\left(g^{\alpha\beta}\partial_\alpha\phi\,\partial_\beta\phi + m^2\phi^2\right). \tag{3.9}$$

Expanding the LHS of Equation 3.8 we have

$$\partial_0\left(\sqrt{-g}\,T^{00}\right) + \partial_i\left(\sqrt{-g}\,T^{ij}\right). \tag{3.10}$$

The first term is the time derivative of the energy density of a co-moving volume element, which is given by

$$\sqrt{-g}T^{00} = \rho(\mathbf{x},t) = \frac{a^3(t)}{2\sqrt{1-kr^2}}\left[\dot{\phi}^2(\mathbf{x},t) + m^2\phi^2(\mathbf{x},t) + \frac{1}{a^2(t)}\left(\delta^{ij} - kx^i x^j\right)\partial_i\phi(\mathbf{x},t)\cdot\partial_j\phi(\mathbf{x},t)\right] \tag{3.11}$$

while the second term in Equation 3.10 represents the spatial flow of particles through the volume element. Substituting for g, $T^{\mu\nu}$, and using the equation of motion (3.7) to remove the $\ddot{\phi}$ term, we find a violation of energy conservation,

$$\dot{\rho}(\mathbf{x},t)+\partial_i\left(\sqrt{-g}\,T^{ij}\right)$$
$$=\frac{a^2(t)\dot{a}(t)}{2\sqrt{1-kr^2}}\left[3\left(m^2\phi^2(\mathbf{x},t)-\dot{\phi}^2(\mathbf{x},t)\right)+\frac{1}{a^2(t)}\left(\delta^{ij}-kx^ix^j\right)\partial_i\phi(\mathbf{x},t)\cdot\partial_j\phi(\mathbf{x},t)\right] \tag{3.12}$$

We are currently examining an inflationary stage of the expanding universe where the Hubble parameter, $H=\dot{a}(t)/a(t)$, is approximately constant. The scale factor grows rapidly during inflation, $a(t) \propto \exp(Ht)$, and thus the spatial fluctuation terms in the equations of motion and co-moving energy density become negligible. Equations 3.7 and 3.11 may then be approximated by

$$\ddot{\phi}(\mathbf{x},t)+3H\dot{\phi}(\mathbf{x},t)+m^2\phi(\mathbf{x},t)\approx 0 \tag{3.13}$$

$$\rho(\mathbf{x},t)\approx\frac{1}{2}a^3(t)\left(\dot{\phi}^2(\mathbf{x},t)+m^2\phi^2(\mathbf{x},t)\right). \tag{3.14}$$

Solving Equation 3.13 for ϕ and substituting into (3.14), we get

$$\rho(\mathbf{x},t)\approx A\exp\left(t\sqrt{9H^2-4m^2}\right)+B\exp\left(-t\sqrt{9H^2-4m^2}\right)+C \tag{3.15}$$

The inflationary stage is thought to have started very shortly after the big bang at $t_{start}\approx 10^{-38}$s, and to have lasted for a very brief time, until $t_{end}\approx 10^{-36}$s. A period of inflation explains several things, such as why the horizon lies beyond the visible universe, why the universe exhibits isotropy and homogeneity on a large scale, and why the CMB contains slight fluctuations. However, inflation must not have been too pronounced, else matter would have been too thinly distributed for structure formation to occur. To satisfy these requirements, $H\Delta t\approx 100$, and thus, during inflation, the Hubble parameter is

$$H\approx\frac{100}{\Delta t}\approx 10^{38}s^{-1}. \tag{3.16}$$

This results in a co-moving energy density for weakly coupled states with $M_X < 1.5H\hbar\approx 10^{23}$eV that is growing exponentially at the end of inflation.

The FRW model assumes that cosmological fluid is composed of three non-interacting components: pressureless gas or "dust," radiation, and vacuum. After

inflation, the scale factor evolves as $a(t) \propto t^{2/l}$, where $l = 3$ for a dust dominated universe, and $l = 4$ if radiation dominates. The Hubble parameter is no longer constant, but becomes

$$\frac{\dot{a}(t)}{a(t)} = \frac{2}{lt} \tag{3.17}$$

and consequently, the equation of motion

$$t\ddot{\phi}(\mathbf{x},t) + \frac{6}{l}\dot{\phi}(\mathbf{x},t) + m^2 t\phi(\mathbf{x},t) \approx 0 \tag{3.18}$$

must be solved using Bessel functions. The general solution is given by

$$\phi(t) = t^{\frac{1}{2}-\frac{3}{l}}\left[A J_{\frac{1}{2}-\frac{3}{l}}(mt) + B J_{\frac{3}{l}-\frac{1}{2}}(mt) \right] \tag{3.19}$$

where A and B are constants (Kamke, 1944).

The asymptotic behaviour of the Bessel functions ($mt >> 1$) is

$$\phi(t) \propto t^{-3/4}\cos(mt + \varphi) \tag{3.20}$$

for radiation, and

$$\phi(t) \propto t^{-1}\cos(mt + \varphi) \tag{3.21}$$

for dust. Using the appropriate values for ϕ and a in Equation 3.14 we get

$$\rho(t) \propto a^3(t)\left(\dot{\phi}^2(t) + m^2\phi^2(t)\right) \propto t^0 . \tag{3.22}$$

From this, we can see that for both radiation and dust, the co-moving energy density of massive particles freezes out at the end of inflation ($t_{end} \approx 10^{-36}$ s) if, at the lower limit,

$$M_X > \frac{\hbar}{t_{end}} \approx 10^{21}\,\text{eV} . \tag{3.23}$$

Thus, a cosmological analysis of particle creation during the inflationary expansion of the early universe results in a mass window on the order 10^{21} to 10^{23} eV for super-heavy relic particles.

3.3 Fragmentation Functions

3.3.1 Motivation for the Use of Fragmentation Functions

The interaction considered for the present analysis is the scenario proposed by Blasi et al. (2002) where the annihilation of dark matter particles produces two jets, each having energy M_x as shown in Figure 3.1. The jets then fragment into multiple particles, which can have energies that are a substantial fraction of M_x. It is postulated that UHECRs are made of these particles, some of which reach the Earth and collide with a particle in the atmosphere, creating a secondary shower of colliding particles. The energy of the primary UHECR particle can be estimated from the size and density of the secondary shower, as discussed in Section 4.3.

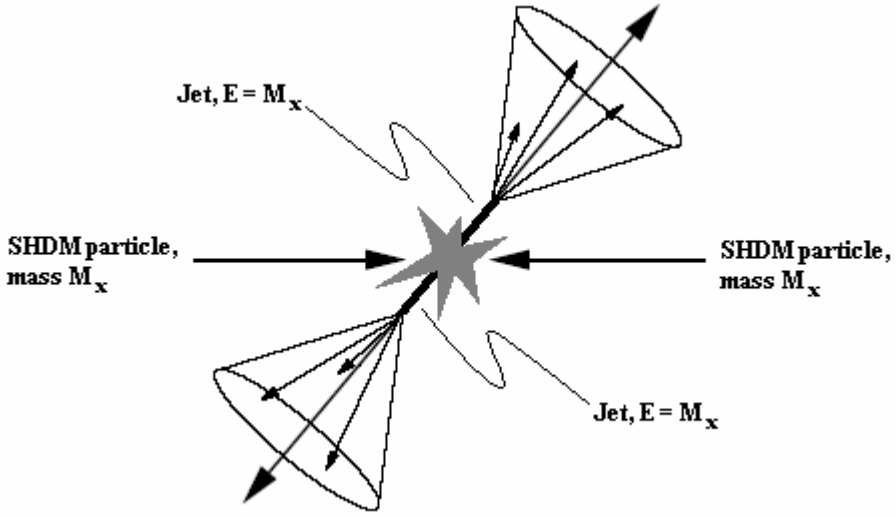

Figure 3.1: Annihilation of two WIMPZILLA particles, resulting initially in two jets of energy M_x which later fragment further.

Over time, the flux of UHECRs at various energies has been measured, providing information about the probability that the fragmenting particles from WIMPZILLA annihilation will have a given energy. Fragmentation functions make predictions about such probabilities based on the centre-of-mass energy of the annihilation event. Though fragmentation functions have only been applied to scattering at much lower energies, they have so far been found to have a universal

form. This leads us to the idea of obtaining information about the annihilation of WIMPZILLAs by fitting the fragmentation function to UHECR spectra.

3.3.2 Definition and Form of the Fragmentation Function

Fragmentation functions, $\frac{dN}{dx}(x,s)$, are dimensionless functions of the QCD-improved parton model which describe the distribution of particle energies resulting from hard scattering processes. $\frac{dN}{dx}(x,s)$ is the probability that a parton jet produced at an energy scale *s* will form a hadron jet that includes a hadron carrying the fraction *x* of the parton jet energy (Biebel et al., 2001; Kniehl et al., 2001). A much earlier proposal for the general form of fragmentation functions was made by Baier et al. (1979) and has since been updated with the addition of a γ term to take the form (Kniehl et al., 2001)

$$\frac{dN}{dx}(x,s) = c_n x^{\alpha}(1-x)^{\beta}\left(1+\frac{\gamma}{x}\right). \tag{3.24}$$

The normalization constant c_n and the parameters α, β, and γ depend on the energy scale, as well as on the type of partons and hadrons involved, and are acquired by fitting Equation 3.24 to a set of data. Frequently, the γ term is omitted, as it is << 1 (e.g. Binnewies et al., 1995; Kniehl et al., 2000; Bourhis et al., 2001), and we too have employed this practice in our analysis.

Assuming two parton jets emerge from a dark matter particle annihilation event with centre-of-mass energy $\sqrt{s}$, the maximum amount of energy that a jet could contain would be $\sqrt{s}/2$. Therefore the fraction of energy of the outgoing hadron would be given by

$$x = \frac{E}{\sqrt{s}/2} \leq 1. \tag{3.25}$$

Since we are considering the annihilation of very massive particles with rest mass M_X, the centre-of-mass energy is

$$\sqrt{s} = E_1 + E_2 = 2M_X \tag{3.26}$$

so the energy fraction is just

$$x = \frac{E}{M_X}. \tag{3.27}$$

As UHECR observatories tend to publish their data as a count of cosmic rays per energy bin, it would be preferable to alter Equation 3.24 to a more useful form. From Equation 3.27, we know

$$\frac{dE}{dx} = M_X \tag{3.28}$$

and thus

$$\frac{dN}{dE} = \frac{1}{M_X}\frac{dN}{dx}. \tag{3.29}$$

The fragmentation spectrum, or differential number of jet components per energy interval, from a jet of energy M_X then becomes

$$\frac{dN(E, M_X)}{dE} = \frac{c_n}{M_X}\left(\frac{E}{M_X}\right)^{\alpha}\left(1 - \frac{E}{M_X}\right)^{\beta}. \tag{3.30}$$

The integral of $E\frac{dN}{dE}$ must recover the total energy for the jet. Thus, the normalization constant c_n arises from the necessity that the following energy sum rule be met:

$$\int_0^{\sqrt{s}/2} dE\, E\frac{dN}{dE} = \frac{\sqrt{s}}{2}. \tag{3.31}$$

In order for the sum rule equation to converge, we must impose the constraint that $\alpha > -2$ and $\beta > -1$.

3.3.3 Universality and Extension to UHECR Regime

Fragmentation functions cannot yet be derived from first principles, but QCD makes two notable predictions about their behaviour (Binnewies, 1997; Kniehl et al., 2001; Biebel et al., 2001). The first is that a fragmentation function can be evolved to different energy scales using the Altarelli-Parisi equations. The second prediction, coming from the factorization theorem, is that fragmentation functions only depend on the outgoing parton jets and on the hadrons produced, not on the

process that produced them. Once a fragmentation function has been fitted to the data from a specific process at a particular centre-of-mass energy, the function can be applied to any process at the same energy due to the universality of factorization. These predictions were tested most recently by Kniehl et al. (2001) by first finding the fragmentation functions for charged pions, kaons, protons and antiprotons from the annihilation of positrons and electrons at $\sqrt{s} = 29\,\text{GeV}$. The analysis was performed on experimental data collected at the Large Electron Positron (LEP1) collider, the Stanford Linear Collider (SLC), and the Positron Electron Project (PEP). They then tested the first prediction by evolving the fragmentation functions to energies ranging from 133 GeV to 189 GeV and comparing their findings to LEP2 e^+e^- annihilation data in this range. An excellent agreement was found between the evolved fragmentation function and experimental data($\chi_\nu^2 \approx 1$). Next, Kniehl et al. tested the second prediction by performing an evaluation of the majority of high-statistics data sets where charged hadrons are produced by colliding beam experiments such as $\gamma\gamma$, γp, $p\bar{p}$ scattering with centre-of-mass energies ranging from 10 to 1800 GeV. Once again, the notion of process independence was strongly upheld by the data.

Fragmentation function universality has so far held for the highest energy events we can produce on Earth. Though this is some eight orders of magnitude lower than the highest energy cosmic rays, we believe that their reliability makes fragmentation functions a reasonable tool to use at UHECR energy regimes.

3.4 Calculation of UHECR Flux

In order to further evaluate the feasibility of the theory that UHECR flux is the result of superheavy dark matter annihilation, it is useful to be able to make a prediction of flux in our region of the galaxy. While comparing annihilation flux from the parent halo with that from subclumps for various halo profiles, Blasi et al. (2002) found that the flux from the subclumps is far greater than that from the halo. We will therefore simplify the flux equation to consider only collisional

annihilation originating in the dense cores of the subclumps. The spectral flux per steradian at the Earth from a compact source of volume V is (Dick et al., 2005)

$$J(E) = \frac{1}{4\pi \,\mathrm{sr}} \cdot \frac{dN(E, M_x)}{dE} \int_V d^3\mathbf{r} \frac{n_x(\mathbf{r})^2 \langle \sigma_A v \rangle \frac{\nu}{4}}{4\pi |\mathbf{r}_\odot - \mathbf{r}|^2}, \tag{3.32}$$

where $\frac{dN(E, M_x)}{dE}$ is the number of jet components per energy interval, as in Section 3.3.2. The number of annihilation events per volume per second will depend upon the number-density of particles, the number-density of antiparticles, and the thermally averaged cross-section: $n_x n_{\bar{x}} \langle \sigma_A v \rangle$. Since we previously adopted the convention that n_x is the total dark matter particle number-density, we must use $\frac{n_x}{2}\frac{n_x}{2}\langle \sigma_A v \rangle$, unless the particles were their own antiparticles (i.e. Majorana particles). We have included a parameter v, which is 4 for Majorana particles and 1 otherwise, to allow for this difference. As the jet particles are taken to be distributed roughly in a spherical shell expanding out from the event, the number of annihilation events is divided by the area of a sphere with a radius equal to the distance from the subclump to the Earth, $4\pi|\mathbf{r}_\odot - \mathbf{r}|^2$. To further simplify Equation 3.32, we assume that the average distance from the Earth to the subclumps is d = 7.3 kpc, based on the mean of the distance-squared to visible galactic substructure, i.e. globular clusters (Dick et al., 2005). We also assume that these substructures have dense cores with a mass density of $n_X m_X$. We then find

$$J(E) = \frac{V}{64\pi^2 d^2} \frac{dN(E, M_x)}{dE} {n_x}^2 \langle \sigma_A v \rangle. \tag{3.33}$$

The total source volume, V, will be given by the number of subclumps in the galaxy multiplied by their average core volume, $N_{cl}\overline{V}_{core}$. N-body models and gravitational lensing indicate that the core accounts for approximately 10% of the average subclump mass, and that a fraction, f_{cl} = 2 to 15%, of the galactic mass lies in substructure (Springel et al, 2001; Chiba, 2002; Stoehr et al, 2002; Hayashi et al, 2003). Thus we have

$$n_X m_X \overline{V}_{core} \approx 0.1\overline{M}_{cl} = \frac{0.1 f_{cl} M_{halo}}{N_{cl}} \Rightarrow N_{cl}\overline{V}_{core} \approx \frac{0.1 f_{cl} M_{halo}}{n_X m_X}. \quad (3.34)$$

We will further parameterize the core density, n_X, of the subclumps in terms of the solar density:

$$n_X = \eta \cdot \frac{\rho_\odot}{m_X} = \eta \frac{7.86 \times 10^{38} \text{ eV}/\text{m}^3 c^2}{m_X} \quad . \quad (3.35)$$

One last simplification of the flux equation may be made by taking the low velocity bounds for the cross section. This is a reasonable approximation since typical velocity dispersions in dark matter halo models are found to be in the range of 10 to 1000 km/s << c. The limit for the cross section then becomes (Hui, 2001)

$$\langle \sigma_A v \rangle = \xi \times \frac{4\pi\hbar^2}{M_x^2 v}, \quad \xi \le 1. \quad (3.36)$$

The simplified equation for flux from dark matter annihilation finally becomes

$$J(E) = v \frac{0.1 f_{cl} M_{halo}}{64\pi^2 d^2 m_X} \eta \frac{\rho_\odot}{m_X} \xi \frac{4\pi\hbar^2}{m_X^2 v} \frac{c_n}{M_X} \left(\frac{E}{M_X}\right)^\alpha \left(1 - \frac{E}{M_X}\right)^\beta, \quad (3.37)$$

or, to facilitate the curve fitting process,

$$J(E) = \frac{n}{M_X} \left(\frac{E}{M_X}\right)^\alpha \left(1 - \frac{E}{M_X}\right)^\beta. \quad (3.38)$$

We would expect $v\eta\xi$ < 1, since ξ must be one or less due to unitarity bound constraints, and η, the ratio of subclump mass density to solar mass density, must be low in order to be consistent with N-body models (e.g. Ghigna et al., 2000; Dalal and Kockanek, 2002; Hayashi et al., 2003). This prediction will be later used as a test of the parameters determined by non-linear curve fits of our model to the UHECR spectra.

3.5 Previous Work Related to UHECRs

Though the UHECR spectrum has not previously been analyzed using fragmentation functions in the context of WIMPZILLA annihilation, there has been some work done on the decay scenario (Fodor and Katz, 2001; Sarkar and

Toldrà, 2002). These works simply make the assumption that the lifetime of decaying particles is greater than the age of the universe. Though the authors cite the creation of sufficiently large quantities of long-lived SHDM particles at the end of inflation, they do not investigate the likelihood of such particles decaying. They also approach the fitting problem quite differently. It is first assumed that UHECRs are protons. They take an existing parameterization of the proton fragmentation function at present accelerator energies (~10^{10} eV) as found by Kniehl et al. (2000) and evolve it up to the UHECR energy regime, using the Altarelli-Parisi equations. On the recommendations of the AGASA Collaboration (e.g. Yoshida et al., 1995), Sarkar and Toldrá assume that the UHECR flux below GZK cut-off is predominantly galactic in origin. It is thought that this component of the spectrum comes from conventional, bottom-up, astrophysical acceleration of particles. In such models, flux is typically found to have a simple power-law relation to energy (i.e. $J \propto E^{\alpha}$ where α = -3.2 ± 0.1). The power-law formula recommended by AGASA is largely based on a perceived "ankle" or change in slope at ~6.3 × 10^{18} eV. UHECR observatories traditionally report a spectral energy range which simply corresponds to a roughly constant exposure value that is instrumentation-dependent and is not a reflection of UHECR physics. Therefore, a best fit of the spectrum is found by superimposing the power-law relation with the evolved fragmentation function, which is expected to dominate the highest-energy region of the spectrum. As recommended by Nagano and Watson (2000), the power-law equation used by Sarkar and Toldá is

$$J(E) = (9.23\times10^{-33}\,\mathrm{m^{-2}s^{-1}sr^{-1}eV^{-1}})\left(\frac{E}{6.3\times10^{18}\,\mathrm{eV}}\right)^{-3.2}. \qquad (3.39)$$

Sarkar and Toldrà estimate SHDM particle mass to be on the order of 10^{21} eV, observing that the decay mass could not be much less than this value and still generate the upper end of the spectrum. Fodor and Katz find a mass range of 8×10^{21} eV to 2×10^{25} eV.

Inspired by Sarkar and Toldrà, our analysis also includes an attempt to fit a combined spectrum as a comparison to a pure fragmentation function fit, using a power-law relation for the lower-energy portion of the spectrum:

$$J(E) = n_{pl}\left(\frac{E}{E_{ankle}}\right)^{\alpha_{pl}} + \frac{n}{M_X}\left(\frac{E}{M_X}\right)^{\alpha}\left(1-\frac{E}{M_X}\right)^{\beta} \quad . \tag{3.40}$$

However, rather than assuming that the fragmentation function should be evolved up from known parameters, we allow all parameters, including those for the power-law term, to be determined by the best fit.

Chapter 4 COLLECTION OF UHECR DATA

4.1 Extensive Air Showers (EAS)

At energies below 10^{12} eV, cosmic rays have a flux of 1 particle per square meter per second or greater (Gaisser, 1990). This flux is high enough to allow direct detection of the primary cosmic ray particles by instruments on board high-altitude balloons or satellites. However, at energies of 10^{18} eV, cosmic ray flux falls to ~1 particle per square km per year, which can no longer feasibly be detected by flying instruments. Instead, information about UHECRs must come from a measurement of the secondary air showers they produce. A primary cosmic ray interacts with a particle high in the atmosphere to generate a shower of particles, with the shower front consisting of a thin disk of relativistic particles. The number of cascading particles initially increases, reaches a maximum, and then decreases as fewer particles have sufficient energy to cause further particle production. This indirect method of UHECR observation introduces many uncertainties, particularly in the estimation of primary particle composition and energy.

As summed up by Malcolm Longair (1992), "…the determination of the chemical composition of cosmic rays with energies greater than $E = 10^{14}$ eV is fraught with problems." The favoured candidates for UHECR primaries are photons, protons, and heavier nuclei. Although theory indicates that air showers caused by these different primary particles should have different characteristics, there is still much dispute over the interpretation of observed air showers.

When a photon primary interacts with an atmospheric particle, it is predicted to be converted into an electron-positron pair (Gaisser, 1990; Longair, 1992). If the energy of the pair is sufficiently high, the particles will produce a secondary photon through Bremsstrahlung radiation when deflected by the field of a nucleus. This secondary photon can potentially produce another electron pair which undergoes further Bremsstrahlung radiation, resulting in an electromagnetic cascade of photons, electrons, and positrons (Figure 4.1). The axis of this shower continues to travel in the direction of the initial photon. Although a high-energy photon could cause the fragmentation of an atmospheric nucleus, this is predicted to be a rare occurrence (Friedlander, 2000). As a result, a photon initiated shower should contain very few muons, pions, and nucleons.

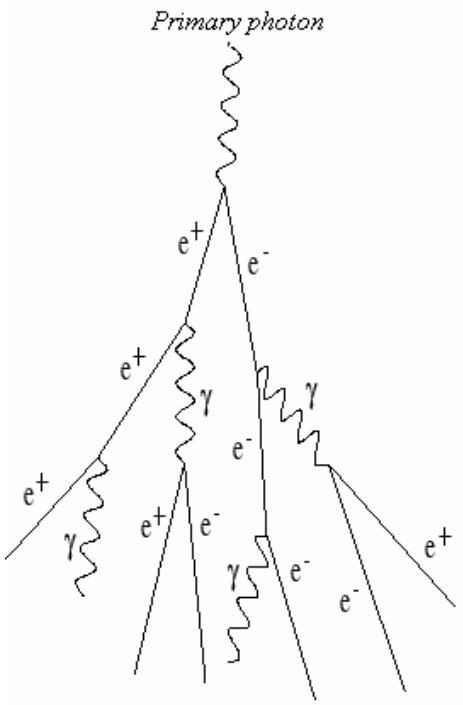

Figure 4.1: The electromagnetic component present in all particle showers. (Adapted from www.gae.ucm.es)

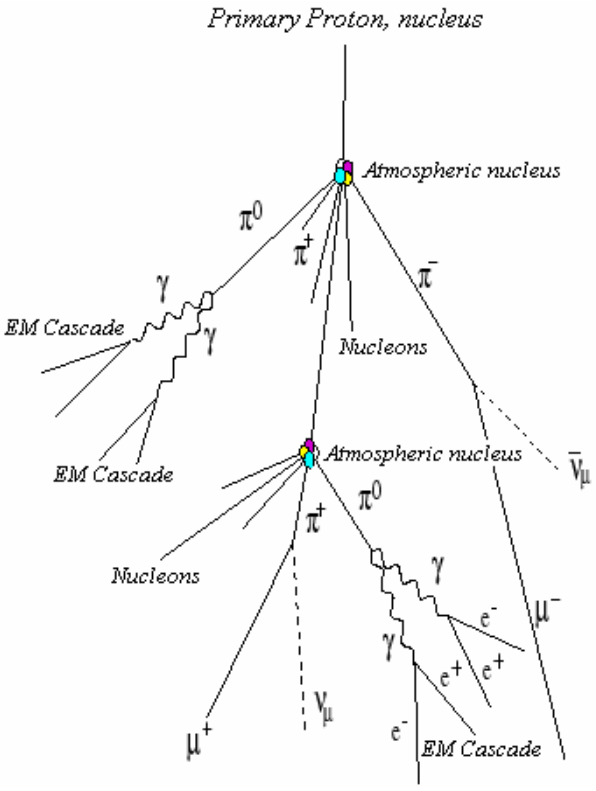

Figure 4.2: Shower produced by proton or heavier nuclei primaries, containing both hadronic and electromagnetic components. (Adapted from www.gae.ucm.es)

In contrast, if a cosmic ray primary is a proton or heavier nucleus, it is thought that the primary will disintegrate when it interacts with an atmospheric nucleus

and these fragments will then have further interactions with other atmospheric particles. If the primary particle energy is high enough, some of the particle fragments may reach the ground. The products of these nuclear disintegrations include pions. The $\pi^{\pm}$ further decay into muons and neutrinos, while the π^0 produces two photons, which initiate electromagnetic showers as described previously. Thus air showers generated by nuclei have both an electromagnetic and a hadronic component (Figure 4.2).

If the primary particle were heavier, such as an iron nucleus, it would have a lower Lorentz factor, $\frac{1}{\sqrt{1-\left(u/c\right)^2}}$, than a proton with the same initial energy. The ensuing generations of particle fragments and decay products would also have lower Lorentz factors, so that the point of maximum shower development should occur higher in the atmosphere than that of a proton primary (Longair, 1992).

Some researchers find an upper limit for photon induced showers with energies around the GZK cut-off to be 50 to 67% (Stecker, 2004). However, protons are generally thought to be responsible for the bulk of secondary air showers having energies over 10^{15} eV, with heavier nuclei causing a smaller percentage and photons potentially producing as few as 1 in 1000 shower events (Nagano and Watson, 2000). As a result, UHECR spectra, including the preliminary Pierre Auger Observatory data, are derived from energy calculations that assume the primary particle is hadronic (E.g. Takeda et al., 2003; Abbasi et al., 2004; Sommers, 2005). However, due to differences in development between photon- and hadron-induced showers, the energy estimates will be too low if the primary particle is actually a photon (Busca et al., 2006). Photon primaries are of particular relevance to this thesis since top-down UHECR source models predict an increase in the photon component above energies of $10^{19.7}$ eV (Berezinksky et al., 1997; Blasi et al., 2002). This region of the UHECR spectrum is particularly susceptible to error due to the very low number of events that have been recorded to date.

4.2 Overview of Ground Detector Array Observatories

The AGASA Observatory recorded observations for over a decade using an array of 111 surface detectors, covering ~100 km^2 about 130 km west of Tokyo (Yoshida et al., 1995). Each detector contained a plastic scintillator, which functioned by absorbing high-energy electromagnetic or charged particle radiation and then releasing the absorbed energy by emitting photons at a characteristic wavelength. The Pierre Auger Observatory significantly increases the rate of events observed on the ground by employing a much larger array of 1600 surface detectors covering 3000 km^2. The Auger detectors consist of 3000-gallon water-Cherenkov tanks. When energetic particles from an EAS pass through the tanks, they travel faster than the speed of light in water, creating an electromagnetic shock wave which displaces electrons in the water medium. The displaced electrons are then restored to equilibrium by the emission of photons, a phenomenon known as Cherenkov radiation. The scintillation light (AGASA) or the Cherenkov radiation (Auger) is then measured by the detector's photomultiplier tube (PMT). Despite the physical differences in the detectors used by the two observatories, the methods used to calculate shower energy are essentially the same.

By the time a secondary shower reaches an observatory, the shower front typically extends over hundreds of meters and will strike several detectors (Figure 4.3). The surface detectors measure the times, locations, and quantities of incoming particles, giving a map of the local particle densities (Figure 4.4). Using differences in timing and variations in particle density, the shower axis is located and the arrival direction is determined to within 1.8° for super-GZK events (Takeda et al., 2003). Based on the work of Hillas et al. (1971), it is assumed that local particle density at a distance of 600 m from the axis of the shower, $S(600)$, is proportional to the energy of the primary particle (Yoshida et al., 1995). The $S(600)$ particle density was chosen as a benchmark because it showed the least amount of variation between the differing shower models.

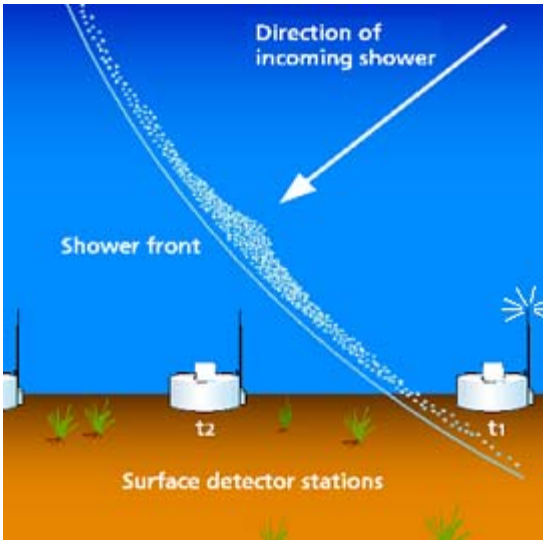

Figure 4.3: Representation of an inclined shower, showing the shower front reaching the detectors at different times (www.auger.org/admin/powerpoint.html).

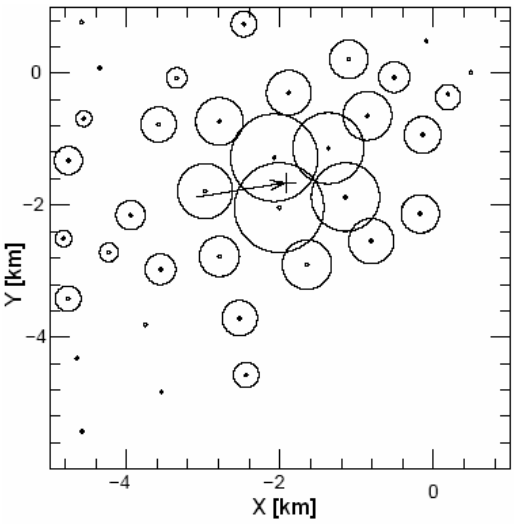

Figure 4.4: Scintillation detectors are denoted by dots, while the radius of the surrounding circle is proportional to the detected particle density. The computed shower axis is indicated by the cross and the shower direction by the arrow (Sakaki et al., 2001).

$S(600)$ is adjusted for shower zenith angle, which effects atmospheric attenuation, giving $S_0(600)$, the $S(600)$ value for a vertically incident shower. Thousands of Monte Carlo simulations were carried out for particle showers resulting from proton and iron primaries, taking into consideration the atmospheric depth of the observatory, shower development theory, and detector response characteristics. These simulations give a range of expected particle densities and shower front patterns for the specified particle type at a given energy. Based on these simulations, the AGASA Collaboration uses the following empirical formula to evaluate UHECR energy (Takeda et al., 2003):

$$E = 2.21\times10^{17} S_0(600)^{1.03}\,\text{eV} \qquad (4.1)$$

Unfortunately, a fairly high degree of uncertainty is associated with the estimation of $S_0(600)$. The most significant contributing factors are fluctuations in shower development in the atmosphere, scintillation detector resolution, and statistical fluctuations in observed shower particles at individual detectors. Because the effect of shower fluctuations grows more pronounced with the zenith angle, showers striking at angles above 45° are discarded. AGASA estimates that the uncertainty in cosmic ray energy is about ±30% for events at 3×10^{19} eV and

±25% for those at 10^{20}eV (Takeda et al., 2003). Largely due to low event statistics, the Pierre Auger Collaboration estimates uncertainties of 30% at 3×10^{18} eV and 50% at 10^{20} eV (Sommers, 2005).

4.3 Overview of Air Fluorescence Observatories

Although this class of observatories is said to measure "air fluorescence," the term is a bit of a misnomer: it is really "scintillation" that is observed. As the energetic charged particles of an EAS travel through the sky, they excite molecules of atmospheric gas, particularly nitrogen. Some of this energy is then emitted as visible and UV light (scintillation) which is collected by the spherical mirrors of the fluorescence telescope and focused on an array of PMTs.

Fluorescence detectors monitor the progress of an air shower front over a portion of its track through the sky and thus can give more information about the shower geometry than ground arrays. However, fluorescence observatories can only operate on clear, moonless nights. The longest-running air fluorescence observatory, HiRes, is located at an altitude of ~4500 ft on a military compound in the Utah desert. Due to low humidity, low average wind speed, and relative isolation from the light pollution generated by urban centres, the location is about as close to ideal as can be found. Even so, the duty cycle is less than 10% (Westerhoff, 2004). In contrast, ground arrays only sample the shower at one depth and must extrapolate primary direction and energy from this. However, ground arrays can operate continuously, monitoring any particle showers that are energetic enough to penetrate through the atmosphere to the observatory location on the ground.

Though the HiRes observatory consists of two air fluorescence telescopes which can potentially observe a given UHECR shower event "in stereo" and thus make a more accurate assessment of shower geometry, the number of events that have actually been observed in stereo is quite low. As a result, the HiRes data set used in this thesis was that collected by a single telescope, HiRes Monocular I, and the

following explanation of shower analysis is based on monocular observations. To combat the problems with stereo measurement, the Pierre Auger Observatory has four air fluorescence measurement stations each consisting of six telescopes (Argirò et al., 2003). The stations are strategically placed throughout the ground detector array to allow for the greatest possible ability to observe an air shower event with both the fluorescence detectors and the ground array (Figure 4.5).

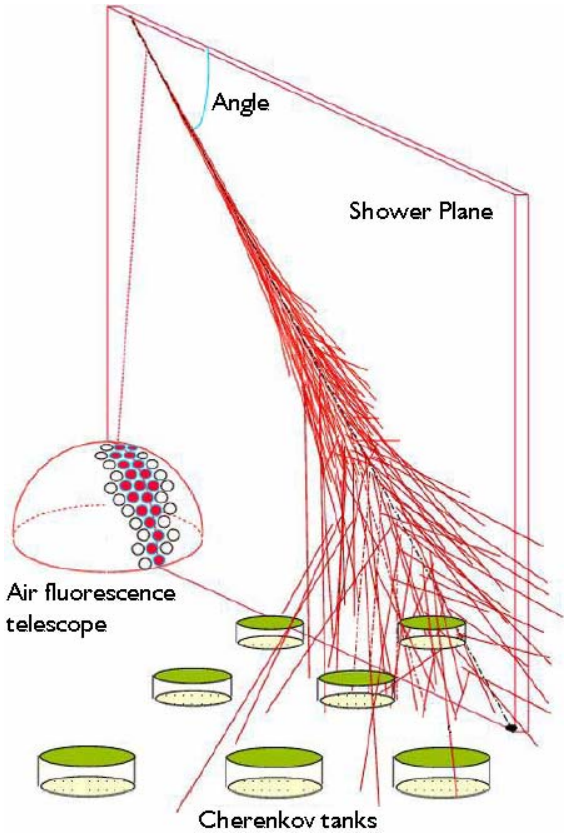

Figure 4.5: Representation of the dual EAS detecting systems at the Pierre Auger Observatory.

For each shower, the fluorescence telescope records the pattern of PMTs fired, and the timing and the intensity of light received (Figure 4.6). The pattern of tubes fired, as well as the angle with which each PMT views the shower, is used to constrain the event to a "shower plane" containing the shower and the detector, as shown in Figure 4.7. The actual trajectory of the shower can then be described by two additional parameters: R_p, the perpendicular distance from the shower axis to the detector, and ψ, the angle of the shower in the shower plane. These

parameters are found by finding a best fit of the measured track to the family of all possible tracks in the plane, considering uncertainties in the instrumentation. As the observed portion of the shower track is relatively short, this step in the shower analysis is the greatest source of error (Bird, et al., 1994; Abu-Zayyad et al., 2001).

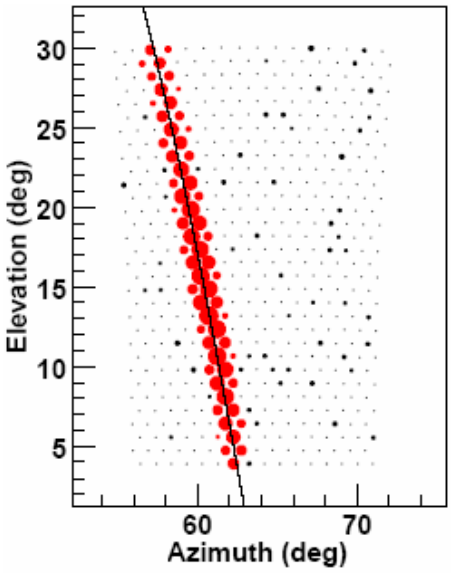

Figure 4.6: Azimuth vs elevation of triggered photomultiplier tubes with a fit of shower-detector plane (Abbasi[1] et al., 2005).

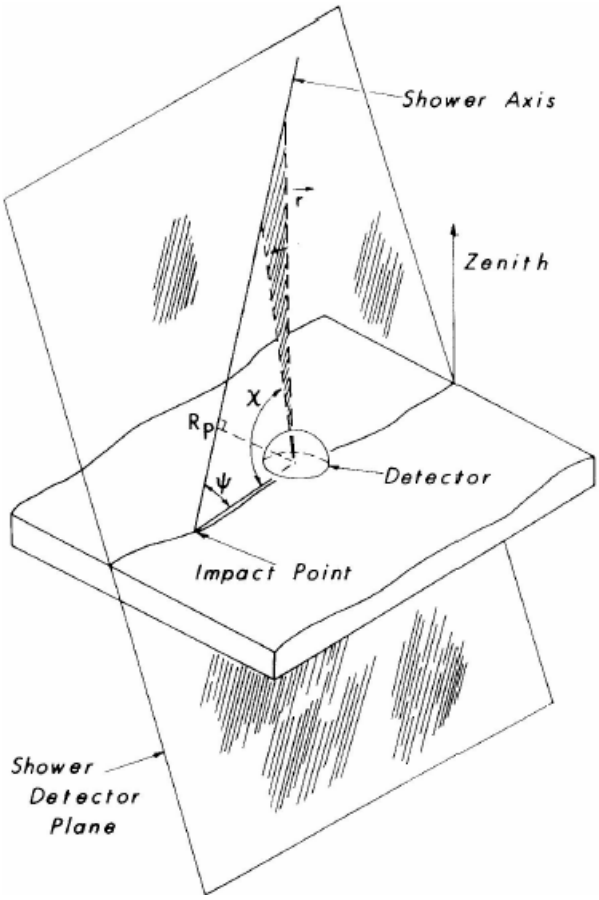

Figure 4.7: Example of shower geometry relative to the HiRes detector (Abbasi[1] et al., 2005).

Once the shower geometry is determined, the recorded light intensity is corrected for $1/r^2$ losses due to the distance between detector and shower, and for attenuation due to interaction with atmospheric particles, which is measured hourly using a calibrated laser signal (Abbasi, et al., 2005). After these adjustments to the recorded shower data, an attempt is made to estimate the energy and composition of the UHECR primary. The Gaisser-Hillas formula

(Gaisser, 1990; Abbasi et al., 2004) predicts the number of electrons in a shower front as a function of primary particle type and atmospheric depth along the shower axis. This formula is incorporated into a Monte Carlo program that also includes a model of detector response to various shower geometries and energies. The shower energy is then determined from the best fit of the Monte Carlo simulations for proton and iron primaries of varying energies to the adjusted observational data. The net result of instrumental, computational, and theoretical uncertainties involved in this indirect method of measurement is that UHECR energy can only be estimated to within 20% at best.

As mentioned in Section 4.1, the primary cosmic ray particle composition may be determined, in theory, from the position of maximum shower development. In practice, there may be substantial fluctuations in shower development, and thus the primary particle type cannot be evaluated for an individual event. Rather, the HiRes team uses slight differences in the average behaviour of particles at different energies to draw conclusions about primary particle composition (Abu-Zayyad, 2001).

4.4 Calculation of UHECR Spectrum from Air Shower Observations

The UHECR spectrum is defined to be the differential flux, $J(E)$, vs. energy, E. The differential flux is the number of cosmic rays observed per area per solid angle per time per energy interval and has units of [m^{-2} sr^{-1} s^{-1} eV^{-1}]. In order to calculate the flux, the aperture, $A\Omega$, (area × solid angle) and observation time for the observatory must be evaluated as a function of primary energy. This is facilitated by the same Monte Carlo simulation program that is used to estimate shower energy (Takeda et al., 2003; Abbasi[1] et al., 2005). Artificial shower events are generated at various energies for an aperture greater than that covered by the observatory, $A_0\Omega_0(E)$. The ratio of the number of events that successfully trigger the modelled detector(s) to the number actually generated is then used to determine the observatory aperture for that energy:

$$A\Omega(E) = A_0\Omega_0 \times \frac{\text{number of triggered events}}{\text{number of generated events}} \tag{4.2}$$

The AGASA and Pierre Auger Observatories find an exposure, which is just aperture × observation time, that is relatively constant for events above 3×10^{18} eV for their ground detection arrays. The exposure for HiRes monocular data changes with energy (see Appendices).

Shower events are divided into energy bins of width ΔE, centred at E_i. If an observatory monitors events for a length of time, T, then the number of events in a given energy bin would be

$$\Delta N_i = T \times \int_{E_i-\Delta E/2}^{E_i+\Delta E/2} dE\, J(E)\, A\Omega(E) \tag{4.3}$$

The energy bins are taken to be sufficiently small relative to the overall energy range measured and thus Equation 4.3 can be approximated by

$$\Delta N_i \approx T\, J(E_i)\, A\Omega(E_i)\Delta E \tag{4.4}$$

which may be manipulated to give a formula for flux (Gaisser, 1990; Abbasi[1] et al., 2005):

$$J(E_i)\left[\text{m}^{-2}\ \text{sr}^{-1}\ \text{s}^{-1}\ \text{eV}^{-1}\right] \approx \frac{\Delta N_i}{T\ A\Omega(E_i)\Delta E}. \tag{4.5}$$

The UHECR spectrum may then be determined by counting the number of events with estimated energies that fall into each energy bin. For comparison, Figure 4.7 shows a plot of the most up-to-date spectra from the three observatories.

4.5 Published Errors in UHECR Spectra

Despite the systematic errors in energy estimation caused by things like shower development theory, detector response, and aperture calculation as mentioned earlier in this chapter, the error bars on published spectra represent only the statistical errors in UHECR measurement. Because cosmic ray flux in the ultra-high-energy regime is so low, the uncertainty due to statistical fluctuations in the

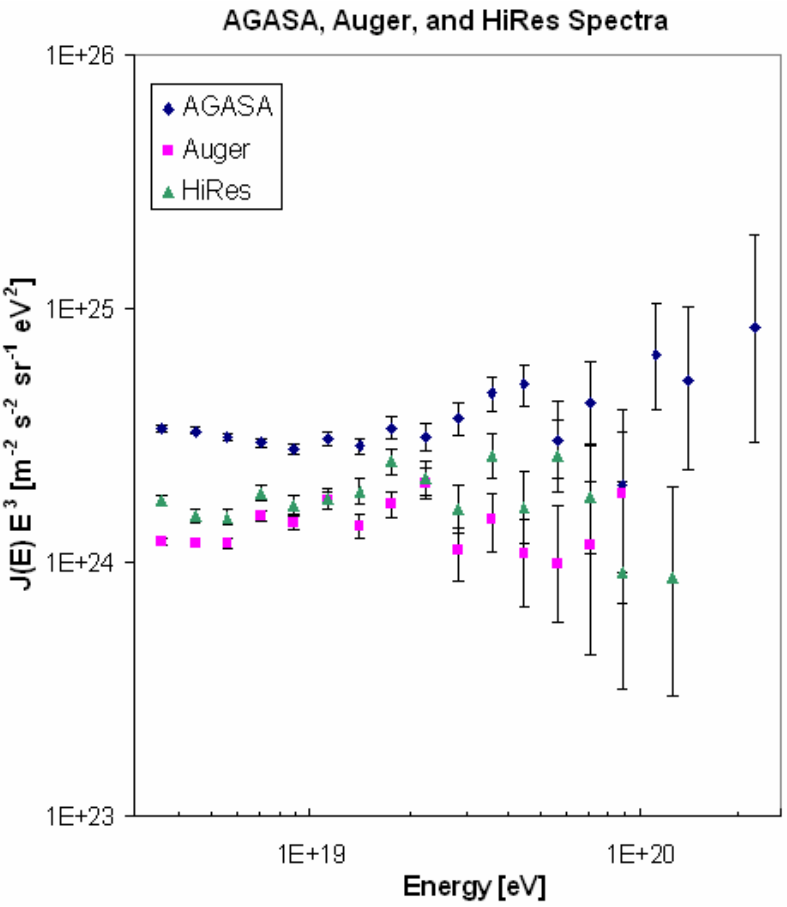

Figure 4.7: UHECR spectra from the AGASA Collaboration in diamonds (Takeda et al., 2003), the High Resolution Fly's Eye Collaboration in triangles (Bergman[2], 2005), and the Pierre Auger Collaboration in squares (Sommers, 2005).

number of observed events heavily outweighs the uncertainty arising from lack of theoretical or instrumental precision. Measurements subject to statistical fluctuations have a Poisson distribution which have the property that the variance of the parent population is equal to the mean, $\sigma^2 = \mu$. For large sample sets, the sample count is sufficiently close to the mean of the parent population that the standard deviation is taken to be the square root of the count (Bevington and Robinson, 2003)

$$\sigma = \sqrt{N} \tag{4.6}$$

To report a "standard error," one would simply use $N \pm \sqrt{N}$.

Propagating the counting error through Equation 4.5, the uncertainty in flux is then represented by

$$\delta J(E_i) = \frac{1}{T\ A\Omega(E_i)\Delta E} \times \sqrt{N_i} \tag{4.7}$$

It must be emphasized that the above equation assumes that there is a sufficiently high number of events per energy bin such that the approximation $\mu \approx N$ holds. Recall, however, that the reason for considering only statistical fluctuations in the calculation of errors for UHECR spectra is that event counts are so low! This conundrum is addressed, at least in part, by the work of Feldman and Cousins (1998) who developed a more reliable set of confidence intervals for low-count data (Table 4.1).

Table 4.1: A comparison between the 68.27% confidence level intervals proposed by Feldman and Cousins (1998) and those predicted by a naïve use of Poisson statistics.

	Feldman and Cousins, 1998		"Poisson"	
N	Minimum count	Maximum count	$N-\sqrt{N}$	$N+\sqrt{N}$
0	0.00	1.29	0.00	0.00
1	0.37	2.75	0.00	2.00
2	0.74	4.25	0.59	3.41
3	1.10	5.30	1.27	4.73
4	2.34	6.78	2.00	6.00
5	2.75	7.81	2.76	7.24
10	6.78	13.81	6.84	13.16
15	11.32	19.32	11.13	18.87
20	15.83	25.30	15.53	24.47

Published UHECR spectra tend to employ the Feldman and Cousins adjustment to error bars for energy bins with event counts of around five or less.

Chapter 5 ANALYSIS

5.1 Curve Fitting

The approach used in curve-fitting is fairly generic. First, an equation believed to model the phenomenon of interest is chosen. This equation will likely have a number of adjustable parameters, so the next step is to select a merit function that provides a quantitative measure of how closely the model output, with a given set of parameters, represents the data collected by observation. It is customary to choose a merit function such that its minimization will yield "best-fit" parameters. Different parameter values are thus evaluated until the merit function reaches a minimum. The goodness of this best fit must then be scrutinized to determine whether the model is a reasonable one.

Observations, however, are imperfect. There is only one correct model that describes a phenomenon, but there are an infinite number of data sets, subject to a variety of measurement and statistical errors, that may arise from observing the phenomenon. The goal is then to maximize the probability of coming up with the observed data set by adjusting model parameters. This is called a maximum likelihood estimation and often takes the form of a least-squares or χ^2-square fit. Of course, if no set of parameters can be found to reasonably duplicate the observed data, then the choice of model must be re-evaluated.

5.2 χ^2-Square Fitting of UHECR Flux Data

We have a set of N measured data points, (E_i, J_i), where E_i is the independent variable, energy, and J_i is the dependent variable, flux. In addition to E-dependence, the model of UHECR flux which is based solely on the

fragmentation function, Equation 3.38, depends non-linearly on four adjustable parameters, $\mathbf{a} = (\alpha, \beta, n, M_X)$; thus $J(E) = J(E; \mathbf{a})$. The combined-spectrum model given by Equation 3.40 includes three additional parameters: $\mathbf{a} = (\alpha, \beta, n, M_X, \alpha_{pl}, n_{pl}, E_{ankle})$. In both cases, α and β must be constrained such that $\alpha > -2$ and $\beta > -1$.

We may assume that the error on each observed data point is random and has a Gaussian distribution around the true value, with the standard deviation at each point being given by σ_i. In this case, the probability that the data set, plus or minus some fixed ΔJ, was generated by the model is the product of the probabilities for each individual point (Press et al., 1992),

$$P \propto \prod_{i=1}^{N} \left\{ \exp\left[-\frac{1}{2}\left(\frac{J_i - J(E_i)}{\sigma_i} \right)^2 \right] \Delta J \right\}. \tag{5.1}$$

This probability is maximized when its logarithm is maximized, i.e. when the negative of its logarithm,

$$\left[\sum_{i=1}^{N} \frac{\left[J_i - J(E_i) \right]^2}{2\sigma_i^2} \right] - N \log \Delta J \,, \tag{5.2}$$

is minimized. Ignoring constants, we find that the most probable parameter set for our model is obtained by minimizing the value of χ^2,

$$\chi^2(\mathbf{a}) \equiv \sum_{i=1}^{N} \left(\frac{J_i - J(E_i; \mathbf{a})}{\sigma_i} \right)^2 . \tag{5.3}$$

Such a minimization is called a least-squares or chi-squared fit of the data.

χ^2 is a valuable tool as it gives a quantitative measurement of the goodness of fit of a model to the observed data. A model has v degrees of freedom, given by v = (number of data points) – (number of equation parameters). The χ^2 statistic has a mean value of v and a standard deviation of $\sqrt{2v}$, therefore a χ^2 value of ~ v represents a good fit. This measure of goodness of fit is usually reported in terms of "reduced χ^2" or $\chi_v^2 = \frac{\chi^2}{v}$. The goal is then to find a fit where $\chi_v^2 \approx 1$.

5.3 The Levenberg-Marquardt Method

Finding the set of parameters that minimizes the merit function can be computationally onerous for models that depend non-linearly on their parameters. An initial estimate of the parameters is input to a procedure which tries to improve the minimization iteratively until χ^2 decreases by less than a specified tolerance. Many different procedures have been developed, but most tend to work well either in the range where the iterative trial parameters are near to or far from the minimum, not in both scenarios. The Levenberg-Marquardt method addresses this issue by switching between the steepest decent method, which excels far from the minimum, and the inverse-Hessian method as the minimum is approached.

If we take **t** to be the current set of P trial parameters (P is either 4 or 7 in our case), the merit function (5.3) can be represented by a Taylor series,

$$\chi^2(\mathbf{a}) = \chi^2(\mathbf{t}) + \sum_i \frac{\partial \chi^2}{\partial a_i}(a_i - t_i) + \frac{1}{2}\sum_{i,j} \frac{\partial^2 \chi^2}{\partial a_i \partial a_j}(a_i - t_i)(a_j - t_j) + \ldots \qquad (5.4)$$

In the inverse-Hessian method, it is assumed that χ^2 is sufficiently close to its minimum that it can be approximated by the quadratic form,

$$\chi^2(\mathbf{a}) \approx \chi^2(\mathbf{t}) + (\mathbf{a}-\mathbf{t})\cdot\nabla\chi^2(\mathbf{t}) + \frac{1}{2}(\mathbf{a}-\mathbf{t})\cdot\mathbf{H}\cdot(\mathbf{a}-\mathbf{t}) \qquad (5.5)$$

where **H** is a $P \times P$ Hessian matrix, the second derivative of χ^2. Equation 5.5 may be rewritten as

$$\nabla\chi^2(\mathbf{a}) = \nabla\chi^2(\mathbf{t}) + \mathbf{H}\cdot(\mathbf{a}-\mathbf{t}). \qquad (5.6)$$

The gradient of χ^2 will be 0 at the minimum, so if the assumption of nearness is reasonable, then the set of parameters that will produce a minimum χ^2, or at least the next best guess, will be given by

$$\mathbf{a}_{\min} = \mathbf{t} - \mathbf{H}^{-1}\cdot\nabla\chi^2(\mathbf{t}). \qquad (5.7)$$

However, if we aren't near to the minimum and χ^2 is not well approximated by Equation 5.5, then the steepest decent method advocates that the quickest way to get closer to the minimum is to take a step down the gradient,

$$\mathbf{a}_{next} = \mathbf{t} - \text{constant}\left(\nabla \chi^2(\mathbf{t})\right) \tag{5.8}$$

ensuring that the constant is small enough that we do not exceed the minimum.

The vector elements of the gradient of χ^2 with respect to the parameters **a**, and the elements of the Hessian matrix, are often rewritten as

$$\beta_k \equiv -\frac{1}{2}\frac{\partial \chi^2}{\partial a_k} \tag{5.9}$$

$$\alpha_{kl} \equiv \frac{1}{2}\frac{\partial^2 \chi^2}{\partial a_k \partial a_l} = \sum_{i=1}^{N} \frac{1}{\sigma_i^2}\left[\frac{\partial J(E_i;\mathbf{a})}{\partial a_k}\frac{\partial J(E_i;\mathbf{a})}{\partial a_l} - \left[J_i - J(E_i;\mathbf{a})\right]\frac{\partial^2 J(E_i;\mathbf{a})}{\partial a_l \partial a_k}\right] \tag{5.10}$$

where $\boldsymbol{\alpha}$ is called the curvature matrix.

Equation 5.7 from the inverse-Hessian method can then be written in terms of a set of linear equations,

$$\sum_{l=1}^{P} \alpha_{kl}\delta a_l = \beta_k \tag{5.11}$$

and the steepest descent Equation 5.8 can also be rewritten

$$\delta a_l = \text{constant} \times \beta_l . \tag{5.12}$$

The Levenberg-Marquardt method capitalizes on the fact that information about the scale of the constant in Equation 5.12 may be obtained from the diagonal elements of the curvature matrix $\boldsymbol{\alpha}$. Employing this idea, Equation 5.12 becomes

$$\delta a_l = \frac{1}{\lambda \alpha_{ll}}\beta_l \qquad \text{or} \qquad \lambda \alpha_{ll}\delta a_l = \beta_l \tag{5.13}$$

where λ is a non-dimensional adjustment factor, used to ensure that the scale factor $\frac{1}{\alpha_{ll}}$ is not so large so as to overshoot the minimum. The Levenberg-Marquardt method then smoothly combines the steepest descent and inverse-Hessian methods by defining a new curvature matrix, $\boldsymbol{\alpha}'$

$$\alpha'_{jj} \equiv \alpha_{jj}(1+\lambda)$$
$$\alpha'_{jk} \equiv \alpha_{jk}, \quad (j \neq k) \tag{5.14}$$

and then replacing Equations 5.11 and 5.13 with

$$\sum_{l=1}^{P} \alpha'_{kl} \delta a_l = \beta_k \, . \tag{5.15}$$

When λ is large, the diagonal terms dominate the new curvature matrix and Equation 5.15 behaves more like the steepest descent method, but as λ approaches zero, it behaves more like the inverse-Hessian method. Based on an initial guess at the parameters, **a**, the best χ^2 is arrived at iteratively as follows:

1. Calculate $\chi^2(\mathbf{a})$.
2. Pick a value for λ.
3. Solve the set of equations (5.14) to find $\delta\mathbf{a}$ and calculate $\chi^2(\mathbf{a} + \delta\mathbf{a})$.
4. If $\chi^2(\mathbf{a} + \delta\mathbf{a}) \geq \chi^2(\mathbf{a})$, increase λ and repeat step 3.
5. If $\chi^2(\mathbf{a} + \delta\mathbf{a}) < \chi^2(\mathbf{a})$, decrease λ, take $\mathbf{a} + \delta\mathbf{a}$ to be the new trial parameters, and return to step 3.

The algorithm is stopped when χ^2 fails to be reduced by a specified tolerance, 10^{-6} in our case. This tolerance value was established by noting that lower values did not substantially refine the parameter set, while taking more computing time.

The curve fitting was performed using two software packages, OriginPro 7.5 (Copyright © 1991-2006 OriginLab Corporation) and IDL Student Edition 6.0.3 (Copyright © 2004, Research Systems Inc.), both of which use the Levenberg-Marquart algorithm as prescribed by Press et al. (1992).

5.4 Error Estimation and Sensitivity Analysis

χ^2 analysis assumes that errors follow a normal or Gaussian distribution, but this is not strictly correct in the measurement of UHECR flux. Flux is a calculated value that contains propagated Poisson-type errors from uncertainties in the count of events occurring in a given energy bin. However, significantly non-normal errors will create an overabundance of outlier data points and will therefore raise

the value of χ^2. Thus, if a reasonable value of χ^2 is achieved in the fitting process, it is a good assumption that the errors essentially follow a normal distribution.

Standard error values for each of the fitted parameters are given by the square root of the diagonal elements of the inverse of the curvature matrix, **α**, as given by Equation 5.10. However, Press et al. (1992) choose to simplify the error calculation for their Levenberg-Marquart algorithm by ignoring the term containing the second derivative of χ^2, thereby deriving the error values from the inverse of

$$\alpha_{kl} = \sum_{i=1}^{N} \frac{1}{\sigma_i^2} \left[\frac{\partial J(E_i;\mathbf{a})}{\partial a_k} \frac{\partial J(E_i;\mathbf{a})}{\partial a_l} \right]. \tag{5.16}$$

It is argued that the term multiplying the second derivative, $\left[J_i - J(E_i;\mathbf{a})\right]$, can be positive or negative and should thus largely cancel out when summed over *i*. In our case, however, it was found that this simplification produced unacceptably high error values and so 1-σ errors were calculated in Maple 8.00 (Copyright © 1981-2002 Waterloo Maple Inc.), using the inverse of matrix produced by Equation 5.10.

A brief sensitivity analysis was performed on the curve fitting algorithm. OriginPro and IDL both require the user to guess at initial values for the parameters that are to be fit. If the first guess is too far away from a reasonable fit, the algorithm fails without producing a fit. Once a workable set of initial values was determined, tests were performed to see whether making small changes to these initial values would affect the final results. We found that the parameters always converged to within a few per cent of the same final solution, and that this variability was less than the error. The results presented in Chapter 6 are those with the lowest χ_v^2.

Chapter 6 RESULTS

6.1 Comparison of Models

For each of the UHECR spectra published by the AGASA, HiRes, and Pierre Auger Observatories, fits of the two models described in Chapter 3 were attempted. The first model assumes that the spectrum is completely dominated by annihilating dark matter particles and thus is governed by the fragmentation function alone (Equation 3.38). The second model postulates that the lower end of UHECR spectra is dominated by particles that are accelerated by powerful astrophysical objects which are predicted to produce a flux that has a simple power-law relation to energy, while the upper end of the spectrum is dominated by dark matter annihilation (Equation 3.40).

It was not possible to achieve a reasonable fit (i.e. one with a low χ_v^2 value) for any of the spectra using the pure fragmentation function model. The results reported in this chapter thus reflect fits of the combined spectrum model only.

6.2 Analysis of the AGASA Spectrum

The most recent AGASA spectrum was published in 2003 (Takeda et al.), a plot of which is shown in Figure 2.4. The numerical data used in the plot is reproduced in Appendix A. UHECR spectra are conventionally shown as $\log(J(E) \times E^3)$ vs. $\log(E)$ in order to flatten the curve and magnify the details of the spectrum at the highest energies. Before a fit of the fragmentation function could be performed, simple calculations were made to adjust the spectrum to $J(E)$ vs. E. The highest and third highest AGASA energy bins, having no observed events, were not included in the analysis.

A χ^2 fit of the AGASA spectrum was then performed, taking the more restrictive error value for σ_i in the case where the positive and negative error values differed. As depicted in Figure 6.1, the fit yielded the following fragmentation function with $\chi^2_\nu = 1.14$:

$$J(E) = 9.9 \pm 1.1 \times 10^{-33}\,\mathrm{m^{-2}s^{-1}sr^{-1}eV^{-1}}\left(\frac{E[\mathrm{eV}]}{6.4 \pm 0.2 \times 10^{18}\,\mathrm{eV}}\right)^{-3.3\pm0.1} + \frac{7.0 \pm 5.7 \times 10^{-17}\,\mathrm{m^{-2}s^{-1}sr^{-1}}}{1.2 \pm 0.6 \times 10^{21}\,\mathrm{eV}}\left(\frac{E[\mathrm{eV}]}{1.2 \pm 0.6 \times 10^{21}\,\mathrm{eV}}\right)^{-1.98\pm0.08} \times \left(1 - \frac{E[\mathrm{eV}]}{1.2 \pm 0.6 \times 10^{21}\,\mathrm{eV}}\right)^{4.6\pm4.3} \quad (6.1)$$

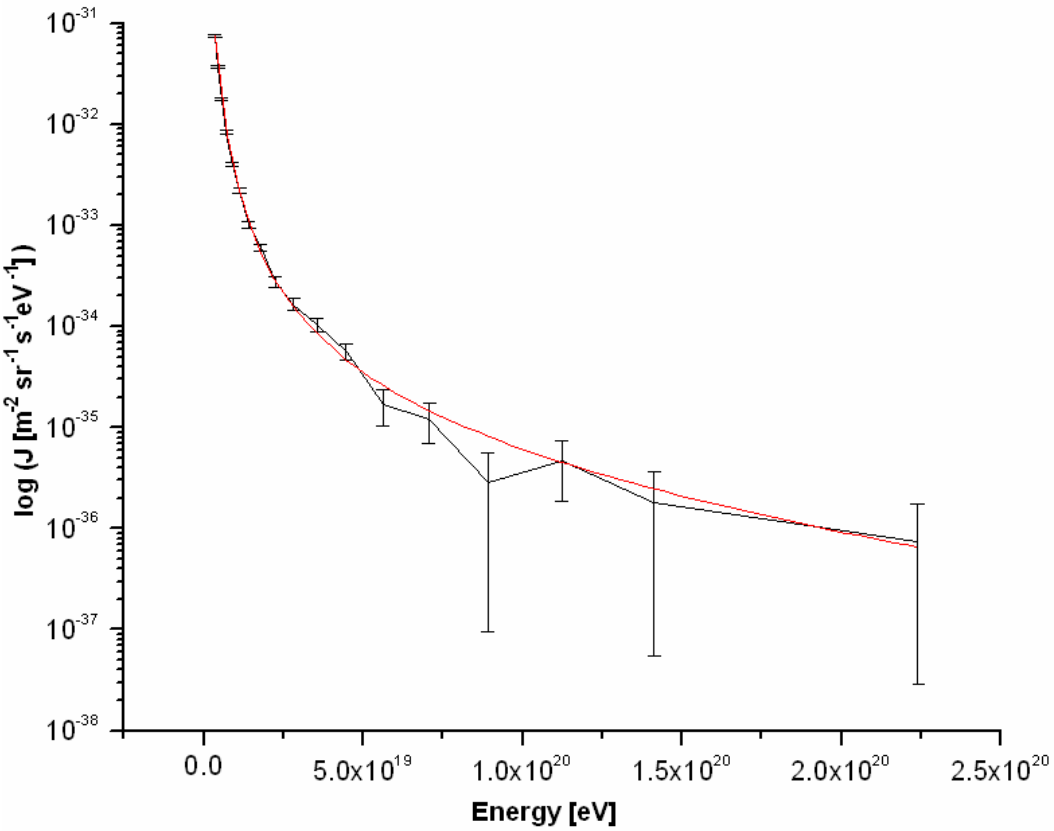

Figure 6.1: Combined power-law and fragmentation function fit, given by smooth red line, to the most recently published AGASA UHECR spectrum, shown as a black segmented line with error bars.

High-energy cosmic ray researchers often refer to a "break" at around 10^{18} where the slope of the spectrum appears to change (e.g. Yoshida et al., 1995). As discussed in Section 3.5, Sarkar and Toldrà (2002) interpreted this change in slope

as a superposition of the spectra of cosmic rays from two different sources. Figure 6.2 shows the contribution to the overall UHECR flux made by each of these components, with the power-law curve computed using the first term in Equation 6.1 and the fragmentation function from the second.

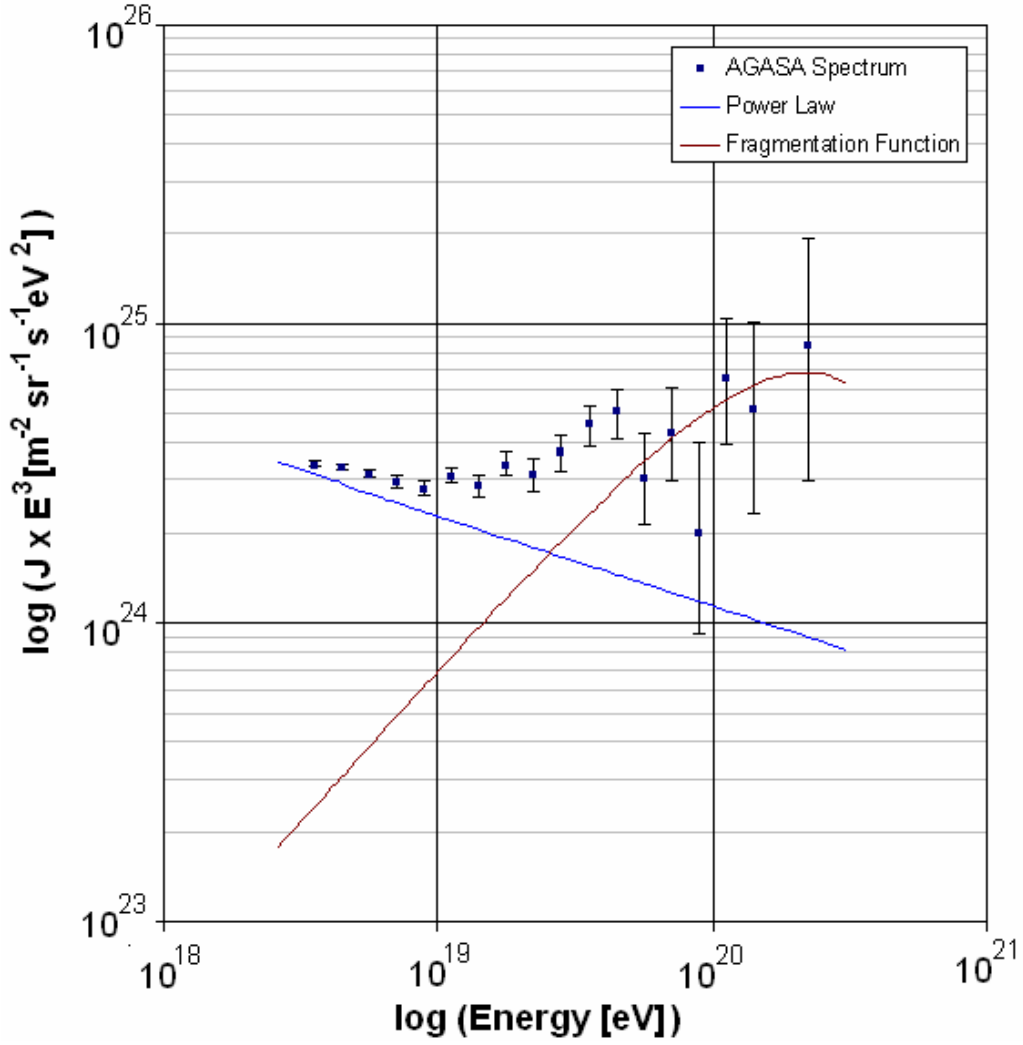

Figure 6.2: Contribution of the two different spectral components to the overall UHECR spectrum reported by AGASA.

Our model proposes that the high-energy end of the UHECR spectrum results from energetic particles coming from dark matter annihilation in galactic halo subclumps. As discussed in Section 2.1.4, much work has been done to characterize dark matter haloes using N-body computer modelling. These studies

provide us with guidelines for the size, quantity, and distribution of galactic subclumps within the context of ΛCDM theory. Using the parameters found by the curve fitting procedure, we may use the flux calculation discussed in Section 3.4 to test whether dark matter subclumps could feasibly produce the UHECR flux observed at Earth. From Equations 3.37 and 3.40, we may compute $v\eta\xi$ by considering only the component of flux which is attributed to annihilation:

$$v\eta\xi = \frac{J(E) - n_{pl}\left(\frac{E}{E_{ankle}}\right)^{\alpha_{pl}}}{\frac{0.1 f_{cl} M_{halo}}{64\pi^2 d^2 m_X}\frac{\rho_\odot}{m_X}\frac{4\pi\hbar^2}{m_X^2 v}\frac{c_n}{M_X}\left(\frac{E}{M_X}\right)^{\alpha}\left(1-\frac{E}{M_X}\right)^{\beta}} \tag{6.2}$$

Extracting average values from N-body models, we take $f_{cl} = 0.1$, $d = 7.3$ kpc, $v =$ 100 km/s, and $M_{halo} = 2 \times 10^{12}\ M_\odot$. The normalization constant c_n is found by solving the energy sum rule (Equation 3.31). At an energy of $10^{19.95}$ eV,

$$(v\eta\xi)_{AGASA} = 0.003\,. \tag{6.3}$$

6.3 Analysis of the HiRes Spectrum

The most recent discussions of the High Resolution Fly's Eye Collaboration spectra were published in 2005 (Abbasi[1] et al., 2005; Bergman[1]). Though these publications included plots of the Hi-Res Monocular I spectrum, they did not contain the data used to create the figures, which instead is located on a web page (Bergman[2], 2005) and reproduced in Appendix B with some modification. The χ^2 fit of the combined spectrum to HiRes data is shown in Figure 6.3 while Figure 6.4 compares the HiRes spectrum with the individual constituents of our model. With a $\chi^2_\nu = 1.78$, the function was found to be:

$$J(E) = 1.3 \pm 1.9 \times 10^{-32}\,\mathrm{m^{-2}s^{-1}sr^{-1}eV^{-1}}\left(\frac{E[\mathrm{eV}]}{4.2 \pm 1.7 \times 10^{18}\,\mathrm{eV}}\right)^{-3.6\pm0.8} +$$

$$\frac{3.0 \pm 0.5 \times 10^{-16}\,\mathrm{m^{-2}s^{-1}sr^{-1}}}{5.0 \pm 4.3 \times 10^{20}\,\mathrm{eV}}\left(\frac{E[\mathrm{eV}]}{5.0 \pm 4.3 \times 10^{20}\,\mathrm{eV}}\right)^{-1.99\pm0.36} \times \left(1 - \frac{E[\mathrm{eV}]}{5.0 \pm 4.3 \times 10^{20}\,\mathrm{eV}}\right)^{13\pm14} \tag{6.4}$$

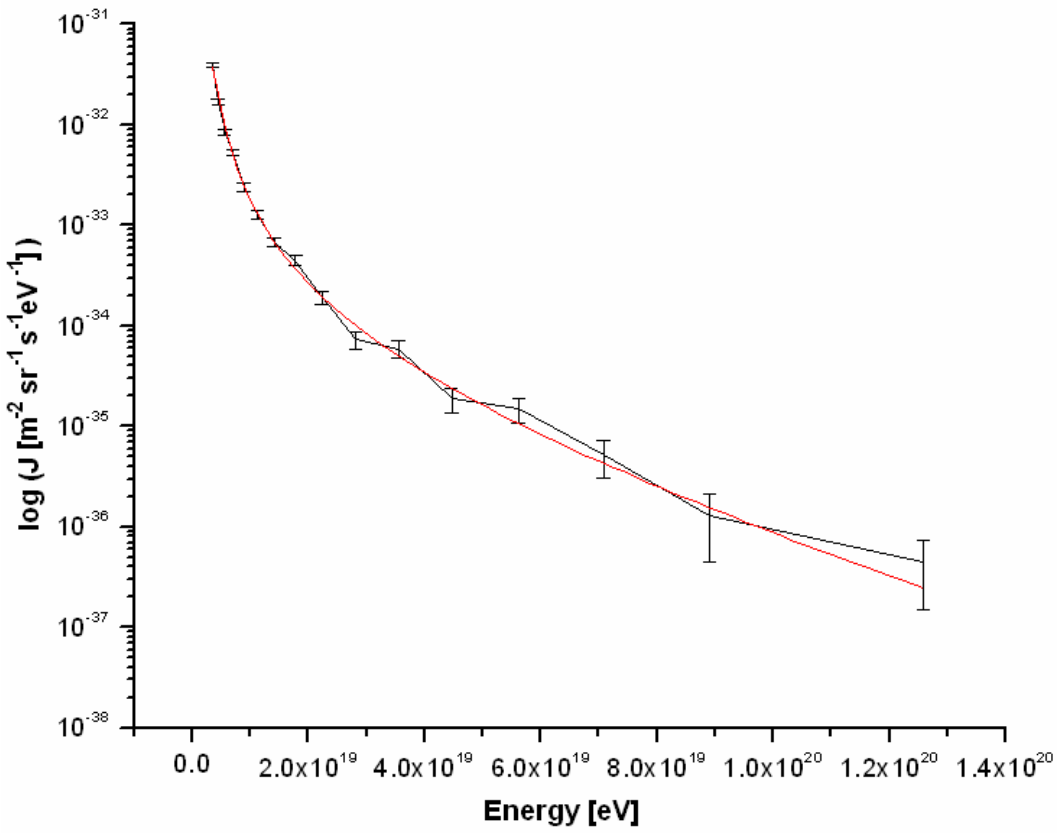

Figure 6.3: The smooth red line shows the superimposed power-law and fragmentation function fit to the HiRes Monocular I data collected from June 1997 to February 2003, shown as a segmented black line with error bars.

Using the parameters found by the curve fitting procedure, we may determine $\nu\eta\xi$ at an energy of $10^{19.95}$ eV to be

$$(\nu\eta\xi)_{HiRes} = 0.006\,. \tag{6.5}$$

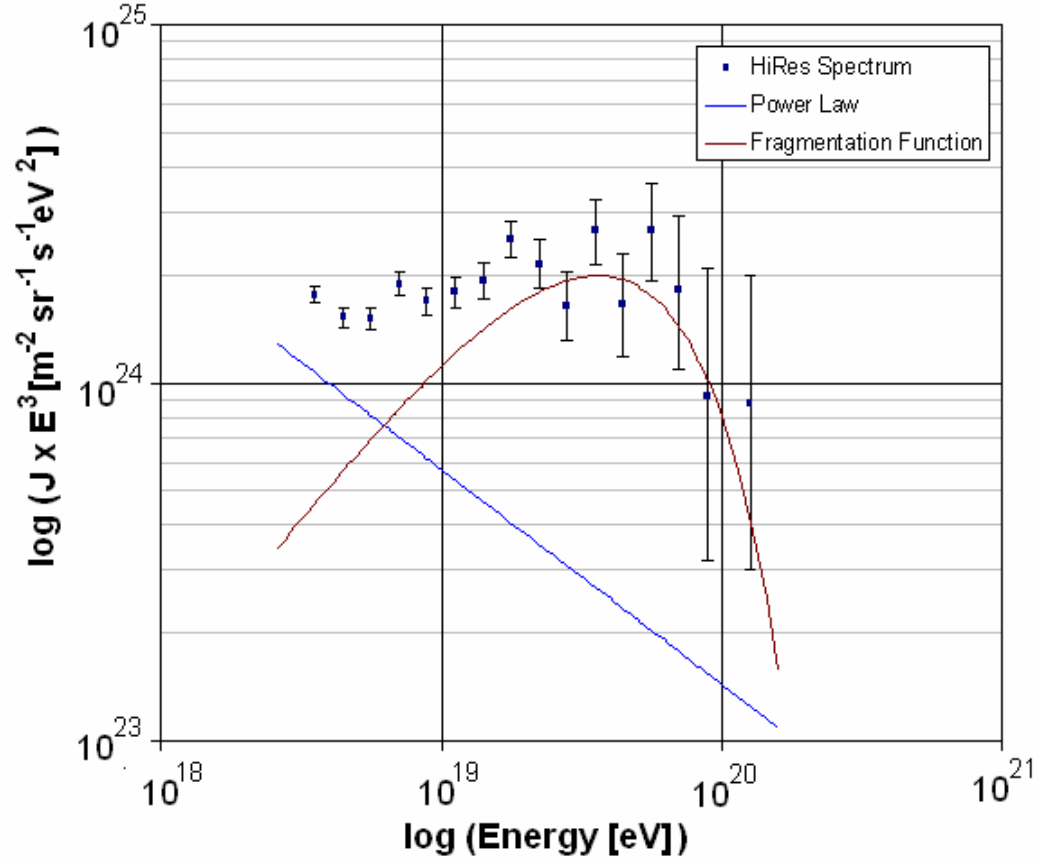

Figure 6.4: Contribution of the two spectral components included in our model to the overall UHECR spectrum published by HiRes.

6.4 Analysis of the Preliminary Auger Spectrum

Preliminary results from the long-awaited Pierre Auger Observatory were released in 2005 by Sommers (see Appendix C). Once again, actual data points were not published, but were extracted from the Pierre Auger web site (Pierre Auger Collaboration, 2005). As shown in Figure 6.5, our fit yielded the following function with $\chi_\nu^2 = 2.60$:

$$J(E) = 2.9 \pm 0.5 \times 10^{-32}\,\mathrm{m^{-2}s^{-1}sr^{-1}eV^{-1}}\left(\frac{E[\mathrm{eV}]}{3.2 \pm 0.2 \times 10^{18}\,\mathrm{eV}}\right)^{-3.1\pm0.1} +$$

$$\frac{9.3 \pm 3.1 \times 10^{-16}\,\mathrm{m^{-2}s^{-1}sr^{-1}}}{2.6 \pm 1.5 \times 10^{21}\,\mathrm{eV}}\left(\frac{E[\mathrm{eV}]}{2.6 \pm 1.5 \times 10^{21}\,\mathrm{eV}}\right)^{-1.48\pm0.03} \times \left(1 - \frac{E[\mathrm{eV}]}{2.6 \pm 1.5 \times 10^{21}\,\mathrm{eV}}\right)^{210\pm160} \quad (6.6)$$

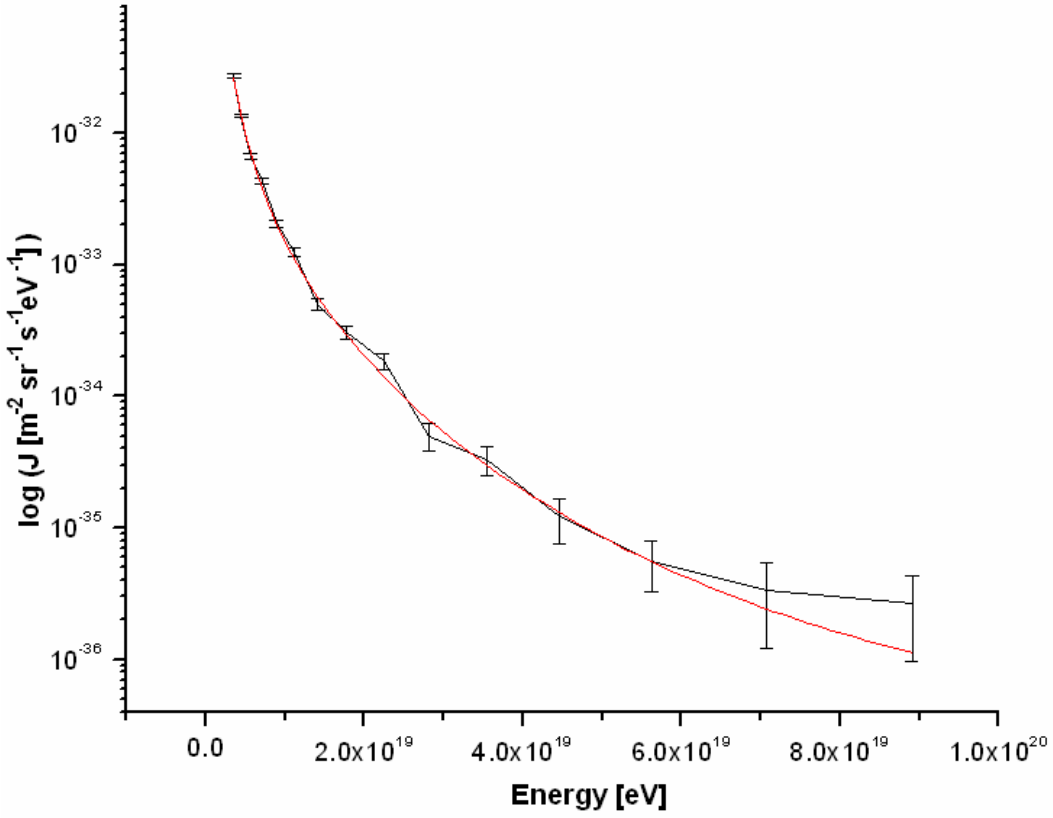

Figure 6.5: Combined spectrum fit, given by smooth red line, to the preliminary Pierre Auger UHECR spectrum, shown as a black segmented line with error bars.

Figure 6.6 compares the power-law and fragmentation function portions of the model spectrum with that reported by the Pierre Auger Observatory. Given the apparent flatness of the Auger spectrum when $J(E) \times E^3$ is plotted against E, a fit of the power-law alone was attempted. This resulted in the function

$$J(E) = 3.6\times10^{-32}\,\mathrm{m^{-2}s^{-1}sr^{-1}eV^{-1}}\left(\frac{E[\mathrm{eV}]}{3.2\times10^{18}\,\mathrm{eV}}\right)^{-2.8}. \tag{6.7}$$

However, the quality of this fit was poorer than that for the combined spectrum, with $\chi^2_\nu = 2.80$. Another model with a two-stage power-law injection spectrum, one for lower energies and one for higher, was also evaluated. It was not possible to obtain a reasonable fit with this model.

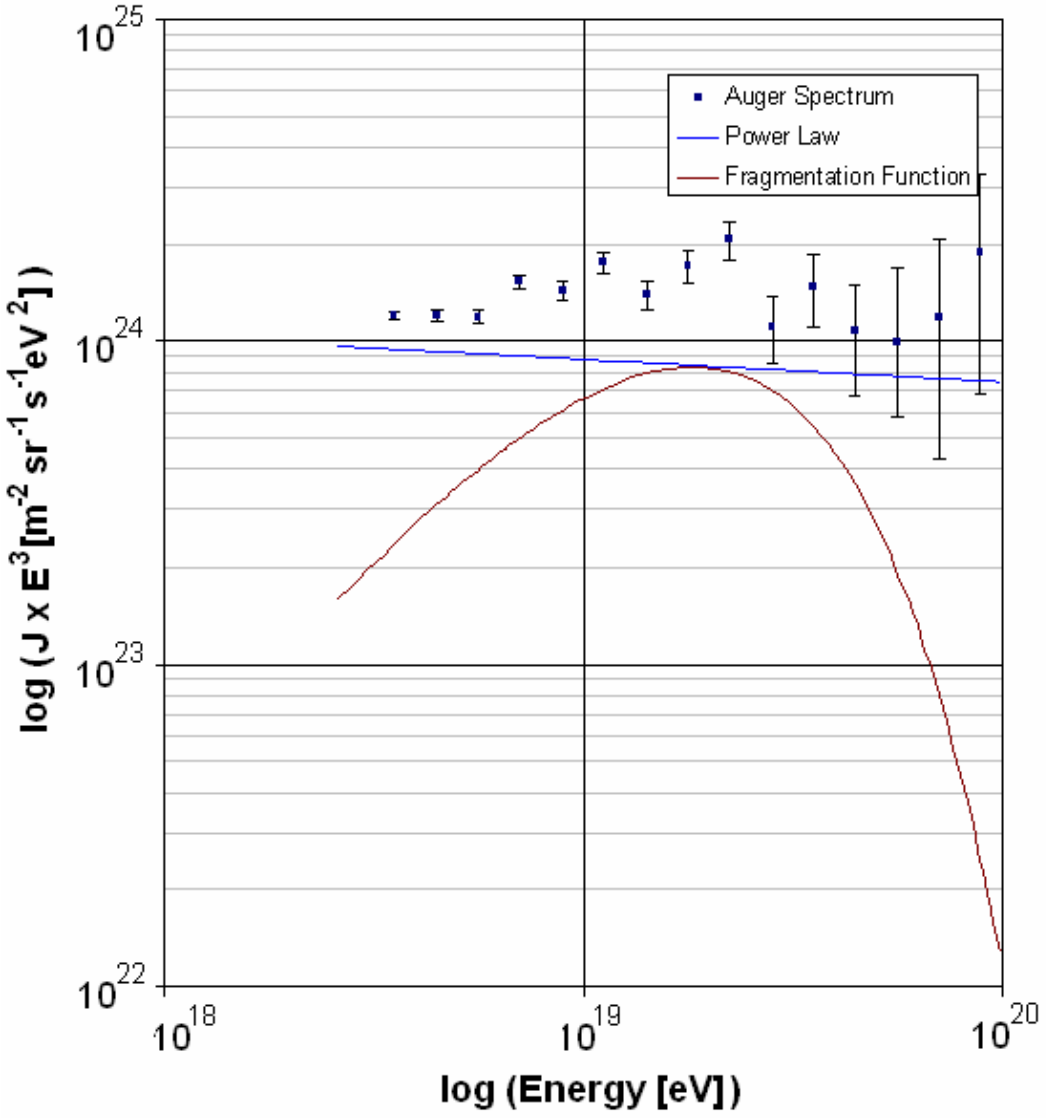

Figure 6.6: Individual components of the model spectrum compared to the Pierre Auger data.

Once again, the parameters found in the curve fit were used to determine $\nu\eta\xi$ at an energy of $10^{19.95}$ eV,

$$\left(\nu\eta\xi\right)_{Auger} = 0.9\,. \tag{6.8}$$

6.5 Summary of Results

For ease of comparison, Table 6.1 summarizes the parameters found in the non-linear curve fits and calculations described in this chapter.

Table 6.1: Summary of parameters derived from fitting a combined low-energy power-law relation superimposed with a fragmentation function (Equation 3.40) to three independent UHECR spectra.

	AGASA	**HiRes**	**Auger**
M_x [eV]	$(1.2 \pm 0.6) \times 10^{21}$	$(5.0 \pm 4.3) \times 10^{20}$	$(2.6 \pm 1.5) \times 10^{21}$
α	-1.97 ± 0.08	-1.99 ± 0.36	-1.48 ± 0.03
β	4.6 ± 4.3	13 ± 14	210 ± 160
n [$m^{-2}s^{-1}sr^{-1}$]	$(7.0 \pm 5.7) \times 10^{-17}$	$(3.0 \pm 0.5) \times 10^{-17}$	$(9.3 \pm 3.1) \times 10^{-16}$
n_{pl} [$m^{-2}s^{-1}sr^{-1}eV^{-1}$]	$(9.9 \pm 1.1) \times 10^{-33}$	$(1.3 \pm 1.9) \times 10^{-32}$	$(2.9 \pm 0.5) \times 10^{-32}$
E_{ankle} [eV]	$(6.4 \pm 0.2) \times 10^{18}$	$(4.2 \pm 1.7) \times 10^{18}$	$(3.2 \pm 0.2) \times 10^{18}$
α_{pl}	-3.3 ± 0.1	-3.6 ± 0.8	-3.1 ± 0.1
χ_v^2	1.14	1.78	2.60
$\nu\eta\xi$	0.003	0.006	0.9

Chapter 7 DISCUSSION

It is perhaps not surprising that we were unable to achieve a good fit of the constrained fragmentation function alone (Equation 3.38) to the published ultra-high-energy cosmic ray spectra. The convention among UHECR observatories is to include cosmic rays with energies above 3.5×10^{18}eV in their reported spectra. This energy range does not reflect any particular theory about UHECR physics; the AGASA Observatory pioneered this convention simply because it is the energy above which their exposure curve becomes fairly constant. However, most researchers believe that cosmic rays come from many different sources, ranging from the sun to unknown galactic and extra-galactic sources (e.g. Hill and Schramm, 1984; Gaisser, 1990; Dova et al., 2001). "Features" in the cosmic ray spectrum, such as dips, bumps, and changes in slope have been pointed to as evidence that the full spectrum as depicted in Figure 2.2 is really composed of overlapping spectra from various sources. Since there appears to be a break in the spectrum at $10^{18.1\pm0.6}$eV, it is reasonable to find that a UHECR flux model based on a single source does not fit well.

The power-law portion of the AGASA fit was found to be the same, within error, as Equation 3.39 used by Sarkar and Toldrá, (2002). Unfortunately, their work on the dark matter decay scenario only involved an analysis of the AGASA spectrum. However, the HiRes Collaboration reports a break in the spectrum at $10^{18.65\pm0.05}$ eV with a slope of -3.17 ± 0.03 below this value (Abbasi[1] et al., 2005). We find the HiRes injection spectrum at the low end to be in agreement with these values. Due to the newness of the data, no published power-law relations were found for the Pierre Auger spectrum.

Although finding agreement between our power-law relations and those determined by other authors helps to validate our fitting methodology, the main goal of this work is to extract information from the fragmentation function portion of the fit in order to test the hypothesis that UHECRs result from dark matter annihilation in the galaxy. In order for the annihilation theory to hold up to this test, it is first necessary to be able to achieve a good fit for our model while constraining the values of α and β. The theory requires that the integral of the energy times the differential number of jet components per energy interval, $E\frac{dN}{dE}$, must recover the total energy for the jet (Equation 3.31). We must constrain $\alpha > -2$ and $\beta > -1$ so that the integral for the energy sum rule may converge. For all three spectra, we were able to obtain a reasonable fit using these constraints.

Another test of our theory is found in whether or not the fit of the fragmentation function produces a reasonable mass value for non-thermal, superheavy dark matter particles. In Section 3.2.2, we outlined a cosmological analysis of dark matter particle production during the inflationary expansion of the early universe performed by Dick et al. (2005). This study found that in order for weakly-interacting, super-heavy particles to still exist in large quantities today, their mass must be on the order of 10^{21} to 10^{23} eV. The fragmentation function fits of the AGASA and Pierre Auger spectra give a mass value within this range, while the HiRes value falls slightly below. Considering that the cosmological analysis is meant to provide only an estimate of mass window, one could argue that the HiRes mass is also in agreement, as the upper end of the 1-σ error range is 9.3×10^{20} eV.

It is also not surprising that we find the HiRes particle mass to be lower than that for the AGASA Collaboration. There has long been a dispute between these two influential observatories over the energy values reported for UHECR events, with

the AGASA Collaboration arguing that the HiRes team's values are too low, and vice versa (see Section 2.2.2). It is perhaps reassuring that the fragmentation function mass for the Auger Observatory data supports the possibility of collisional annihilation, as this observatory purports to settle the disagreement between HiRes and AGASA. What is not so reassuring is the quality of our fit to the Auger spectrum, which gives a reduced χ^2 value that, while acceptable, was higher than that for the other two observatories. One can visualize the difficulties with the Auger fit by comparing the plots of the individual power-law and fragmentation function components of our model to the published spectra (Figures 6.2, 6.4, and 6.6). In the AGASA and HiRes plots, the contribution of the power-law component decreases rapidly with increasing energy, as predicted. However, the Auger spectrum is much flatter when plotted as $J(E) \times E^3$ vs. E, and has an ill-defined ankle. As a result, the power-law component of our model has a greater overall contribution at high energies, which was not expected. However, the combined power-law/fragmentation function spectrum still provides a superior fit to that for simple power-law relations, indicating that bottom-up acceleration is unlikely to provide a full explanation for the entire UHECR spectrum. The Pierre Auger data set used in our analysis is still quite small and the methodology used in their energy calculations is still being refined. The shape of the spectrum may change significantly once more UHECR events have been processed. However, if the Auger spectrum does not eventually evolve to have similar characteristics to the AGASA and HiRes spectra, it would be wise to devise a new model.

Annihilation involves an interaction between two particles of energy M_X and we model the annihilation event as initially producing two jets, also having energy M_X, which then fragment further. As a result, we may directly compare the masses that we calculate with those found in past work on dark matter particle decay as a source of UHECRs. As discussed in Section 3.5, Sarkar and Toldrà (2002) analysed the AGASA spectrum, while Fodor and Katz (2001) studied a composite spectrum of "normalized" data from AGASA, HiRes, Fly's Eye, and Haverah Park, though what "normalized" means in this case is not discussed.

Both groups assume that UHECR primaries are protons and use the Altarelli-Parisi equations to evolve existing parameterizations of the fragmentation function up to UHECR energies. With this method, Sarkar and Toldrá find a mass ~10^{21}eV while Fodor and Katz give a mass window of 8×10^{21} to 2×10^{25}eV. While we agree with the former estimate, our mass values fall below the latter. One potential explanation for this discrepancy is that the Fly's Eye data would have included the highest-energy UHECR ever recorded at 3.2×10^{20}eV, while the highest energy bin for the data that we analysed was 2.2×10^{20}eV. A spectrum with a higher maximum energy might increase the mass value predicted by the fragmentation function.

Our final test of the annihilation theory involves estimating dark matter subclump particle density that would be required to produce the observed UHECR flux. By using the combined-spectrum parameters found by in the curve fits, information from N-body models of a CDM universe, and UHECR observatory data, we may reduce the equation for predicted flux discussed in Section 3.4 down to three unknown parameters, $\nu\eta\xi$ (Equation 6.2). While we cannot yet solve for the individual variables, we know that their product must be << 1. Depending on whether WIMPZILLAs are Majorana particles or not, ν is either 4 or 1 respectively. ξ must be less than one due to unitarity bounds, and η, the ratio of the core mass density of dark matter subclumps to the density of the sun, must be less than one to be consistent with ΛCDM models. We find that AGASA and HiRes values for $\nu\eta\xi$ are well within this limit and therefore provide further support for the annihilation theory. The Pierre Auger data yields $\nu\eta\xi = 0.9$, which is a little too close to one for comfort. Upon further analysis of Equation 6.2, we realize that varying β may greatly influence the value calculated for $\nu\eta\xi$. For the Auger spectrum, β has a large uncertainty, ranging from 50 to 370. This β range yields values for $\nu\eta\xi$ as low as 0.007, which supports the annihilation proposal, to 150, which refutes the theory. Once again, the preliminary nature of the Auger data and the ensuing uncertainty in the fit of our model prevent us from drawing conclusions about annihilation based on the Auger spectrum.

Chapter 8 CONCLUSIONS

We have obtained reasonably good fits of our combined-spectrum model to data from the three most important UHECR observatories: the Akeno Giant Air Shower Array, the High Resolution Fly's Eye, and the Pierre Auger Observatories. This leads us to suggest that cosmic rays in the "ultra-high" energy regime come from at least two different sources. The lower end of the spectrum is dominated by sources producing a flux that decreases with energy in a simple power law relation. This type of behaviour is more consistent with theories in which primary UHECR particles derive their energy from being accelerated by powerful astrophysical forces. The high end of the UHECR spectrum exhibits the characteristics one would expect to see from the fragmentation of extremely massive particles. Given that UHECR arrival directions are relatively isotropic and that ΛCDM models of the universe show an abundance of substructure in the dark matter halo, we predict that the highest energy UHECRs come from the annihilation of exotic, superheavy dark matter particles residing in the dense cores of halo subclumps.

The fragmentation function model allows us to obtain a relatively precise estimate of dark matter particle mass. Taking the outer limits of the ranges of mass values obtained from non-linear curve fits of the combined-spectrum model to data from the three observatories, we find $1\times10^{20}\text{eV} < M_X < 4\times10^{21}\text{eV}$. We are encouraged that this range overlaps with previous estimates, both from similar work on the dark matter decay scenario and from a cosmological analysis. We are also heartened by the fact that the fitted fragmentation function parameters yield credible subclump particle densities. Conversely, the slightly poorer fit of our

combined-spectrum model to the Pierre Auger data indicates that more work needs to be done in evaluating this paradigm. Certainly, we look to future reports from the Auger Observatory to resolve the discrepancies between the various spectra though preliminary indications are promising for collisional annihilation as a source of UHECRs.

Chapter 9 RECOMMENDATIONS FOR FUTURE WORK

First and foremost, future releases of Pierre Auger data must be scrutinized as they become available. As the Auger Collaboration refines techniques for UHECR primary energy estimation and as the event counts become more statistically significant, two criteria must be met in order for the collisional annihilation source model to survive. Perhaps the most immediately telling test is that one must begin to see small scale anisotropy in UHECR arrival directions, as only the cores of dark matter subclumps achieve particle densities conducive to annihilation. The other criterion is that there should be an improved fit for a flux model, of which the fragmentation function is a component, to the Auger spectrum. As more and more events are recorded, it would perhaps be a useful exercise to reduce the size of spectral energy bins, which are currently as high as 5×10^{19}eV, to search for previously undetectable features and to once again test the quality of a fragmentation function fit.

While waiting for the accumulation and processing of data by the Auger Observatory, further work to test our model could be performed. Other researchers have evaluated the possible link between dark matter particle fragmentation and UHECRs by making assumptions about the composition of UHECR primaries and evolving existing, particle-specific parameterizations of the fragmentation function up to UHECR energies using the Alterelli-Parisi equations. It is thought that dark matter particle annihilation should predominantly produce photon primaries. Therefore, it would be interesting to take the fragmentation functions that we have obtained from our non-linear curve

fits and evolve them down to current particle collider energies. By comparing these evolved functions to those determined experimentally, we may discover something about the composition of primary particles.

Another idea for further work may be obtained from methods used by UHECR observatories to estimate cosmic ray energy. There exists a model for the development and characteristics of extended air showers caused by primary particles of various compositions. UHECR researchers run thousands of Monte Carlo simulations of these air showers for cosmic rays having various energies and arrival directions. They then search for the most significant match between predicted and actual measurements in order to characterize the cosmic ray. Since errors in UHECR flux are statistical in nature, perhaps we should attempt a more statistical approach to curve fitting. A large number of Monte Carlo simulations of the UHECR spectrum could be generated for different parameterizations of the fragmentation function, using the results presented in Chapter 6 as a starting point. One could then search for the most likely match of a particular parameterization to the published spectra. The curve-fitting method employed in this thesis assumes a Gaussian error distribution, which, while a reasonable assumption, is not strictly correct. A statistical analysis method may produce more accurate results.

LIST OF REFERENCES

R.U. Abbasi et al. (HiRes Collaboration), 2004, "Measurement of the Flux of Ultrahigh Energy Cosmic Rays from Monocular Observations by the High Resolution Fly's Eye Experiment," Phys.Rev.Lett., 92:151101

R.U. Abbasi[1] et al. (HiRes Collaboration), 2005, "Monocular Measurement of the Spectrum of UHE Cosmic Rays by the FADC Detector of the HiRes Experiment," Astropart. Phys., 23:157

R.U. Abbasi[2] et al. (HiRes Collaboration), 2005, "Search for Point-Like Sources of Cosmic Rays with Energies above 10^18.5 eV in the HiRes-I Monocular Data-Set," Submitted to Elsevier Science, astro-ph/0507663

T. Abu-Zayyad et al. (HiRes Collaboration), 2001, "Measurement of the Cosmic Ray Energy Spectrum and Composition from 10^{17} to $10^{18.3}$ eV Using a Hybrid Fluorescence Technique," Astrophys. J., 557:686

S. Argirò, et al. (Pierre Auger Collaboration), 2003, "Performance of the Pierre Auger Fluorescence Detector and Analysis of Well Reconstructed Events," Proceedings of the 28th International Cosmic Ray Conferences, Tsukuba, Japan, 457

N.A. Bahcall, J. P. Ostriker, S. Perlmutter, P.J. Steinhardt, 1999, "The Cosmic Triangle: Assessing the State of the Universe," Science, 284:1481

R. Baier, J. Engels, B. Petersson, 1979, "Symmetric Hadron Pairs at Large Transverse Momenta as a Test of Hard Scattering Models," Z. Phys. C, Particles and Fields, 2:265

C. L. Bennett et al., 2003, "First Year Wilkinson Microwave Anisotropy Probe (WMAP) Observations: Preliminary Maps and Basic Results," Astrophys. J. Suppl., 148:1

V. Berezinsky, M. Kachelrieß, A.Vilenkin, 1997, "Ultra-High Energy Cosmic Rays Without GZK Cutoff," Phys. Rev. Lett., 97:4302

D. Bergman[1] (HiRes Collaboration), 2005, "Fitting the Hires Spectra," Proceedings of the 29th International Cosmic Ray Conference, Pune, India, 101

D. Bergman[2] (HiRes Collaboration), 2005, http://www.physics.rutgers.edu/~dbergman/HiRes-Monocular-Spectra.html and personal correspondence

L. Bergström, 2000, "Non-Baryonic Dark Matter: Observational Evidence and Detection Methods," Rep. Prog. Phys., 63:793

G. Bertone, D. Hooper, J. Silk, 2005, "Particle Dark Matter: Evidence, Candidates and Constraints," Phys. Rept., 405:279

P. R. Bevington, D. K. Robinson, 2003, Data Reduction and Error Analysis, McGraw-Hill, New York, pp 142-164

O. Biebel, P. Nason, B.R. Webber, 2001, Bicocca-FT-01-20, Cavendish-HEP-01/12, MPI-PhE/2001-14, hep-ph/0109282

J. Binnewies, B.A. Kniehl, G. Kramer, 1995, "Next-to-Leading Order Fragmentation Functions for Pions and Kaons," Z.Phys. C, 65:471

J. Binnewies, 1997, "Fragmentation Functions in Next-To-Leading Order QCD," Hamburg University PhD Thesis, DESY 97-128

D. J. Bird et al. (Fly's Eye Collaboration), 1994, "Detection of a Cosmic Ray with Measured Energy Well Beyond the Expected Spectral Cutoff Due to Cosmic Microwave Radiation," Astrophys.J., 424:491

P. Blasi, R. Dick, E.W. Kolb, 2002, "Ultra-High Energy Cosmic Rays from Annihilation of Superheavy Dark Matter," Astropart. Phys., 18:57

L. Bourhis, M. Fontannaz, J.Ph. Guillet, M. Werlen, 2001, "Next-to-Leading Order Determination of Fragmentation Functions," Eur. Phys. J. C, 19:89

N. Busca, D. Hooper, E. W. Kolb, 2006, "Pierre Auger Data, Photons, and Top-Down Cosmic Ray Models," Phys.Rev. D 73:123001

M. Chiba, 2002, "Probing Dark Matter Substructure in Lens Galaxies," Astrophys. J., 565:17

N. Dalal, C.S. Kockanek, 2002, "Direct Detection of Cold Dark Matter Substructure," Astrophys. J., 572:25

R. Dick, K. M. Hopp, K. E. Wunderle, 2005, "Ultrahigh Energy Cosmic Rays from Collisional Annihilation Revisited," Can. J. Phys., 83(11):1141

M. T. Dova, L. N. Epele, J. D. Swain, 2001, "Massive Relic Neutrinos in the Galactic Halo and the Knee in the Cosmic Ray Spectrum," Proceedings of the 27th International Cosmic Ray Conference, Hamburg, 1780

G. R. Farrar, 2005, "A Cluster of Ultrahigh Energy Cosmic Rays", astro-ph/0501388

G. Feldman, R. Cousins, 1998, "A Unified Approach to the Classical Statistical Analysis of Small Signals," Phys. Rev. D, 57:3873

Z. Fodor, S.D. Katz, 2001, "Grand Unification Signal from Ultra High Energy Cosmic Rays?," Phys.Rev.Lett., 86:3224

M. W. Friedlander, 2000, A Thin Cosmic Rain: Particles from Outer Space, Harvard University Press, Cambridge, Massachusetts, pp. 103-125

T. K. Gaisser, 1990, Cosmic Rays and Particle Physics, Cambridge University Press, Great Britain, pp. 193-262

S. Ghigna et al., 2000, "Density Profiles and Substructure of Dark Matter Halos: Converging Results at Ultra-High Numerical Resolution," Astrophys. J., 544:616

K. Greisen, 1966, "End to the Cosmic-Ray Spectrum," Phys. Rev. Lett., 16:748

E. Hayashi, J.F. Navarro, J.E. Taylor, J. Stadel, T. Quinn, 2003, "The Structural Evolution of Substructure," Astrophys. J., 584:541

C. Hill, D. Schramm, 1985, "Ultrahigh-Energy Cosmic-Ray Spectrum," Phys. Rev. D, 31:564

A. M. Hillas, 1984, "The Origin of Ultra-High-Energy Cosmic Rays," Ann. Rev. Astron. Astrophys., 22:425

A. M. Hillas, D. J. Marsden, J. D. Hollows, H. W. Hunter, 1971, "Measurement of Primary Energy of Air Showers in the Presence of Fluctuations," Proceedings of the 12th International Cosmic Ray Conference, Hobart, 3:1001

L. Hui, 2001, "Unitarity Bounds and the Cuspy Halo Problem,"Phys. Rev. Lett., 86:3467

E. Kamke, 1944, Differentialgleichungen Lösungsmethoden und Lösungen, Chelsea Publishing Company, New York, pp438-441

A. Klypin, A.V. Kravtsov, O. Valenzuela, F. Prada, 1999, "Where are the Missing Galactic Satellites?," Astrophys. J., 522:82

B. A. Kniehl, G. Kramer, B. Pötter, 2000, "Fragmentation Functions for Pions, Kaons, and Protons at Next-to-Leading Order," Nucl. Phys. B, 582:514

B. A. Kniehl, G. Kramer, B. Pötter, 2001, "Testing the Universality of Fragmentation Functions," Nucl. Phys. B, 597:337

S. P. Knurenko, et al. (Yakutsk Collaboration), 2005, "Spectrum of Cosmic Rays with Energy Above 10^{17}eV," Int. J. Mod. Phys., A20:6878

E. W. Kolb, D. J. H. Chung, A. Riotto, 1999, "WIMPZILLAS!," Dark Matter in Astrophysics and Particle Physics, H. V. Klapdor-Kleingrothaus, L. Baudis (Eds.), IoP Publishing, Bristol, pp592-611

M. S. Longair, 1992, High Energy Astrophysics, Vol. 1, Cambridge University Press, Great Britain, pp. 120-154, 284-291

S. Mao, P. Schneider, 1998, "Evidence for Substructure in Lens Galaxies?", MNRAS, 295:587

B. Moore et al., 1999, "Dark Matter Substructure Within Galactic Halos," Astrophys. J., 524:L19

B. Moore et al., 2001, "Dark Matter in Draco and the Local Group: Implications for Direct Detection Experiments," Phys. Rev. D, 64:063508

M. Nagano, A. A. Watson, 2000, "Observations and Implications of the Ultrahigh-Energy Cosmic Rays," Rev. Mod. Phys., 72:689

A. V. Olinto, 2004, "Rapporteur Talk for UHERCs: Messengers of the Extreme Universe," Proceedings of the 28th International Cosmic Ray Conferences, Tsukuba, Japan, 1

J. P. Ostriker, P. Steinhardt, 2003, "New Light on Dark Matter," Science, 300:1909

Pierre Auger Collaboration, 2005, http://www.auger.org/icrc2005/spectrum.html

W. H. Press, S. A. Teukolsky, W. T. Vetterling, B. P. Flannery (Eds.), 1992, Numerical Recipes in C, Cambridge University Press, Cambridge, pp 656-703

N. Sakaki et al. (AGASA Collaboration), 2001, "Cosmic Ray Energy Spectrum Above 3 x 10^{18}eV," Proceedings of the 27th International Cosmic Ray Conference, Hamburg, 1:333

S. Sarkar, R. Toldrá, 2002, "The High Energy Cosmic Ray Spectrum from Relic Particle Decay," Nucl. Phys. B, 621:495

P. Sommers (Pierre Auger Collaboration), 2005, "First Estimate of the Primary Cosmic Ray Energy Spectrum Above 3 EeV from the Pierre Auger Observatory," Proceedings of the 29th International Cosmic Ray Conference, Prune, India, 101

V. Springel, S.D.M. White, G. Tormen, G. Kauffmann, 2001, "Populating a Cluster of Galaxies - I. Results at z = 0," MNRAS, 328:726

F.W. Stecker, 2004, "Ultrahigh Energy Cosmic Rays: Old Physics or New Physics," Nucl. Phys. B, C136:309

T. Stanev, R. Engel, A. Muecke, R. J. Protheroe, J. P. Rachen, 2000, "Propagation of Ultra-High Energy Protons in the Nearby Universe," Phys. Rev. D, 62:93005

F. Stoehr, S.D.M. White, G. Tormen, V. Springel, 2002, "Milky Way's Satellite Population in a ΛCDM Universe," MNRAS, 335:L84

M. Takeda et al. (AGASA Collaboration), 1998, "Extension of the Cosmic-Ray Energy Spectrum Beyond the Predicted Greisen-Zatsepin-Kuz'min Cutoff," Phys. Rev. Lett., 81:1163

M. Takeda et al. (AGASA Collaboration), 1999, "Small-Scale Anisotropy of Cosmic Rays Above 10^{19}eV Observed with the Akeno Giant Air Shower Array," Astrophys. J., 522:225

M. Takeda, et al. (AGASA Collaboration), 2003, "Energy Determination in the Akeno Giant Air Shower Array Experiment," Astropart. Phys., 19:447

A. Tasitsiomi, 2003, "The Cold Dark Matter Crisis on Galactic and Subgalactic Scales", Int. J. Mod. Phys., D12:1157

Y. Uchihori et al., 2000, “Cluster Analysis of Extremely High Energy Cosmic Rays in the Northern Sky,” Astrophys. J., 13:151

S. van den Burgh, 1999, “The Early History of Dark Matter,” PASP 111:657

S. Westerhoff (HiRes Collaboration), 2004, “Search for Small-Scale Anisotropy of Cosmic Rays Above 10^{19} eV with HiRes Stereo,” Nucl. Phys. B (Proceedings Suppl.), 136C:46

S. Yoshida, et al. (AGASA Collaboration), 1995, “The Cosmic Ray Energy Spectrum Above 3 x 10^{18} eV Measured by the Akeno Giant Air Shower Array,” Astropart. Phys., 3:105

G.T. Zatsepin, V.A. Kuz'min, 1966, “Upper Limit of the Spectrum of Cosmic Rays,” JETP Lett., 4:78

APPENDIX A: AGASA COLLABORATION SPECTRUM

Takeda et al., 2003

Published:				**Calculated:**				
Energy, log(E)	**Adjusted Flux, log($J(E)\times E^3$)**	**Adjusted Flux Error (-)**	**Adjusted Flux. Error (+)**	**Energy, E**	**Energy Bin Width**	**Flux, J**	**Flux Error (-)**	**Flux Error (+)**
log([eV])	**[m^{-2} s^{-1} sr^{-1} eV^2]**	**[m^{-2} s^{-1} sr^{-1} eV^2]**	**[m^{-2} s^{-1} sr^{-1} eV^2]**	**[eV]**	**[eV]**	**[m^{-2} s^{-1} sr^{-1} eV^{-1}]**	**[m^{-2} s^{-1} sr^{-1} eV^{-1}]**	**[m^{-2} s^{-1} sr^{-1} eV^{-1}]**
18.55	24.528	0.009	0.009	3.55E+18	8.19E+17	7.55E-32	1.55E-33	1.58E-33
18.65	24.519	0.011	0.010	4.47E+18	1.03E+18	3.71E-32	9.27E-34	8.63E-34
18.75	24.497	0.013	0.013	5.62E+18	1.30E+18	1.77E-32	5.21E-34	5.37E-34
18.85	24.473	0.017	0.016	7.08E+18	1.63E+18	8.38E-33	3.22E-34	3.14E-34
18.95	24.449	0.022	0.021	8.91E+18	2.06E+18	3.97E-33	1.96E-34	1.97E-34
19.05	24.492	0.026	0.025	1.12E+19	2.59E+18	2.20E-33	1.28E-34	1.30E-34
19.15	24.460	0.034	0.032	1.41E+19	3.26E+18	1.02E-33	7.71E-35	7.82E-35
19.25	24.530	0.041	0.038	1.78E+19	4.10E+18	6.03E-34	5.43E-35	5.51E-35
19.35	24.496	0.054	0.048	2.24E+19	5.17E+18	2.79E-34	3.27E-35	3.26E-35
19.45	24.568	0.064	0.056	2.82E+19	6.50E+18	1.65E-34	2.26E-35	2.27E-35
19.55	24.664	0.073	0.062	3.55E+19	8.19E+18	1.03E-34	1.60E-35	1.58E-35
19.65	24.702	0.089	0.074	4.47E+19	1.03E+19	5.65E-35	1.05E-35	1.05E-35
19.75	24.484	0.153	0.146	5.62E+19	1.30E+19	1.71E-35	5.09E-36	6.85E-36
19.85	24.633	0.161	0.154	7.08E+19	1.63E+19	1.21E-35	3.75E-36	5.15E-36
19.95	24.304	0.340	0.294	8.91E+19	2.06E+19	2.84E-36	1.54E-36	2.75E-36
20.05	24.814	0.219	0.203	1.12E+20	2.59E+19	4.61E-36	1.83E-36	2.75E-36
20.15	24.711	0.340	0.294	1.41E+20	3.26E+19	1.82E-36	9.90E-37	1.77E-36
20.25	*24.779			1.78E+20	4.10E+19			
20.35	24.924	0.449	0.364	2.24E+20	5.17E+19	7.48E-37	4.82E-37	9.82E-37
20.45	*25.177			2.82E+20	6.50E+19			

* Estimate of adjusted flux. No cosmic ray events were observed in this energy bin.

AGASA exposure, AΩT, for energy bins:	log(E[eV]) = 18.55 to 18.65 (estimated):	4.7×10^{16} [m^2 s sr]
	log(E[eV]) = 18.75 to 18.95 (estimated):	5.0×10^{16} [m^2 s sr]
	above log(E[eV]) = 19 (published):	5.1×10^{16} [m^2 s sr]

APPENDIX B: HIGH RESOLUTION FLY'S EYE COLLABORATION

MONOCULAR I SPECTRUM (June 1997 – February 2003)

D. Bergman,[2] 2005

Published:						**Calculated:**			
Energy, log(*E*)	**Number of Events**	**Exposure × d*E***	**Flux, *J***	**Flux, Lower Limit**	**Flux, Upper Limit**	**Energy, *E***	**Energy Bin Width**	**Flux Error (-)**	**Flux Error (+)**
log([eV])		**[m^2 s sr eV] × 10^{-30}**	**[m^{-2} s^{-1} sr^{-1} eV^{-1}] × 10^{30}**	**[m^{-2} s^{-1} sr^{-1} eV^{-1}] × 10^{30}**	**[m^{-2} s^{-1} sr^{-1} eV^{-1}] × 10^{30}**	**[eV]**	**[eV]**	**[m^{-2} s^{-1} sr^{-1} eV^{-1}]**	**[m^{-2} s^{-1} sr^{-1} eV^{-1}]**
18.55	390	9894	0.03940000	0.03741000	0.04150000	3.55E+18	8.19E+17	1.99E-33	2.10E-33
18.65	272	15900	0.01705000	0.01602000	0.01815000	4.47E+18	1.03E+18	1.03E-33	1.10E-33
18.75	211	24920	0.00849100	0.00790700	0.00911500	5.62E+18	1.30E+18	5.84E-34	6.24E-34
18.85	203	38150	0.00532700	0.00495400	0.00572800	7.08E+18	1.63E+18	3.73E-34	4.01E-34
18.95	137	57220	0.00238700	0.00218300	0.00260800	8.91E+18	2.06E+18	2.04E-34	2.21E-34
19.05	107	84270	0.00126700	0.00114500	0.00140200	1.12E+19	2.59E+18	1.22E-34	1.35E-34
19.15	83	122100	0.00068120	0.00060650	0.00076410	1.41E+19	3.26E+18	7.47E-35	8.29E-35
19.25	78	174400	0.00044630	0.00039600	0.00050300	1.78E+19	4.10E+18	5.03E-35	5.67E-35
19.35	47	245700	0.00019160	0.00016390	0.00022380	2.24E+19	5.17E+18	2.77E-35	3.22E-35
19.45	25	342200	0.00007326	0.00005861	0.00009114	2.82E+19	6.50E+18	1.47E-35	1.79E-35
19.55	28	471600	0.00005933	0.00004810	0.00007289	3.55E+19	8.19E+18	1.12E-35	1.36E-35
19.65	12	643800	0.00001863	0.00001335	0.00002577	4.47E+19	1.03E+19	5.28E-36	7.14E-36
19.75	13	871500	0.00001490	0.00001077	0.00002029	5.62E+19	1.30E+19	4.13E-36	5.39E-36
19.85	6	1171000	0.00000513	0.00000308	0.00000821	7.08E+19	1.63E+19	2.05E-36	3.08E-36
19.95	2	1562000	0.00000129	0.00000045	0.00000296	8.91E+19	2.06E+19	8.40E-37	1.67E-36
20.10	2	4791000	0.00000044	0.00000015	0.00000100	1.26E+20	1.00E+20	2.90E-37	5.60E-37

APPENDIX C: PIERRE AUGER COLLABORATION SPECTRUM

Sommers, 2005

Published:			**Calculated:**					
Energy, log(*E*)	**Number of Events**	***E*×*J***	**Energy, *E***	**Energy Bin Width**	**Flux, *J***	**Flux Error (-)**	**Flux Error (+)**	**Exposure**
log([eV])		**[km^{-2} sr^{-1} yr^{-1}]**	**[eV]**	**[eV]**	**[m^{-2} s^{-1} sr^{-1} eV^{-1}]**	**[m^{-2} s^{-1} sr^{-1} eV^{-1}]**	**[m^{-2} s^{-1} sr^{-1} eV^{-1}]**	**[m^{2} s sr]**
18.55	1216	3.01	3.55E+18	8.19E+17	2.70E-32	7.75E-34	7.75E-34	4.89916E+16
18.65	766	1.89	4.47E+18	1.03E+18	1.35E-32	4.87E-34	4.87E-34	4.91498E+16
18.75	478	1.18	5.62E+18	1.30E+18	6.68E-33	3.06E-34	3.06E-34	4.91248E+16
18.85	388	0.96	7.08E+18	1.63E+18	4.32E-33	2.19E-34	2.19E-34	4.90135E+16
18.95	233	0.57	8.91E+18	2.06E+18	2.04E-33	1.33E-34	1.33E-34	4.9572E+16
19.05	178	0.44	1.12E+19	2.59E+18	1.25E-33	9.36E-35	9.36E-35	4.90594E+16
19.15	92	0.22	1.41E+19	3.26E+18	4.96E-34	5.17E-35	5.17E-35	5.07131E+16
19.25	71	0.17	1.78E+19	4.10E+18	3.04E-34	3.61E-35	3.61E-35	5.06482E+16
19.35	53	0.13	2.24E+19	5.17E+18	1.85E-34	2.54E-35	2.54E-35	4.9441E+16
19.45	18	0.044	2.82E+19	6.50E+18	4.97E-35	1.17E-35	1.17E-35	4.96106E+16
19.55	15	0.037	3.55E+19	8.19E+18	3.32E-35	8.57E-36	8.57E-36	4.91637E+16
19.65	7	0.017	4.47E+19	1.03E+19	1.21E-35	4.58E-36	4.58E-36	4.99349E+16
19.75	4	0.0099	5.62E+19	1.30E+19	5.61E-36	2.33E-36	3.90E-36	4.89982E+16
19.85	3	0.0074	7.08E+19	1.63E+19	3.33E-36	2.11E-36	2.55E-36	4.91637E+16
19.95	3	0.0074	8.91E+19	2.06E+19	2.64E-36	1.67E-36	2.03E-36	4.91637E+16